STUDIES OF INDUCTIVE PLASMAS AND THEIR APPLICATION TO THETA-PINCH DEVICES VIA NUMERICAL MODELING

by

WARNER CHARLES MEEKS

A THESIS

Presented to the Faculty of the Graduate School of the

MISSOURI UNIVERSITY OF SCIENCE AND TECHNOLOGY

In Partial Fulfillment of the Requirements for the Degree

MASTER OF SCIENCE IN AEROSPACE ENGINEERING

2012

Approved by

Joshua L. Rovey, Advisor
Kakkattukuzhy M. Isaac
Carlos H. Castano

ABSTRACT

First, a globally-averaged RF plasma model is used to investigate exit conditions immediately following a RF pre-ionization stage. Analysis shows that reducing pulse duration from 10^{-6} to 10^{-7} seconds increases peak ion energy fraction by 17% (from 16 to 33%) and doubles final conductivity. Pulse waveforms are square in nature, and ion energy fraction is defined in this work as the percentage of total input energy entrained in ions. Increasing total energy deposition from 5 to 160 mJ increases ion energy fraction from 33% to 58% at a 200 ns pulse duration. This increase is not linear however, showing instead a diminishing return with a peak fraction plateau estimated at 65% to 70%. A constant (time-average) power analysis reveals that, across all power levels (10 to 100 kW), energies (5 mJ to 1 joule), and durations (0.05 to 10 μs), peak ion energy fraction consistently occurs approximately 1 to 2 μs before peak conductivity.

Second, single particle and particle-in-cell simulations are used to elucidate breakdown physics in a ringing theta-pinch with bias magnetic field. The analyses presented here agree with previously conducted experimental results showing that gas breakdown occurs only upon approximate nullification of the bias magnetic field by the pulsed theta-pinch magnetic field. Parametric analysis of the peak electron energy as a function of the bias and pre-ionization magnetic fields reveals that; 1.) when bias magnetic field is ≈ 97% of the pre-ionization magnetic field the peak electron energy is highly erratic, and 2.) high electron energy levels require a pre-ionization to bias magnetic field ratio of 2 to 1 or higher. This second work went on to be published in the Phys. of Plasmas Journal, Vol. 19 (2012, http://link.aip.org/link/doi/10.1063/1.4717731).

ACKNOWLEDGEMENTS

Professionally, I would like to thank my advisor, Dr. Joshua Rovey. In addition to assisting in my research he helped to craft my abilities as a researcher and problem solver. Thanks to Dr. Mitat Birkan and the Air Force Office of Scientific Research (AFOSR grant# FA9550-10-1-0204) as well as the Office of Graduate Studies (providing the Chancellor's Fellowship program) for helping to make this research possible. To Dr. David Kirtley, Dr. Dan Brown, Carrie Hill, and Dr. Scott Kovaleski for sharing their valuable insights and experiences. To Sudhakar Mahalingam, Dr. John Verboncoeur, and the members of the OOPIC User's Group for their advice and insights regarding the implementation of XOOPIC. Also thanks to my committee members Dr. Isaac and Dr. Castano for helping me to realize my goal of obtaining a graduate level education.

Personally, I would like to thank Dr. Rovey for his support as a friend. Raising a family whilst pursuing an advanced degree presents challenges and pressures that he understands and relates to. While at the same he has kept pressure on me to see my goals to the end.

Finally, I would like to thank my wife for putting up with the late nights at work and the lack of patience at times. Jamie, through thick and thin, your love is apparent and gives me strength.

TABLE OF CONTENTS

Page

LIST OF ILLUSTRATIONS

Page

LIST OF TABLES

Page

NOMENCLATURE

Symbol	Description
B_{bias}	bias magnetic field magnitude
B_{net}	net magnetic field magnitude
B_{PI},B_{main}	magnetic field magnitude of stage immediately following bias
B_x	magnetic field in Cartesian $\hat{x}$-direction
D	characteristic diameter
D_{eff}	effective diffusion coefficient
e	fundamental charge
E_{abs}	energy absorbed by system
E_{ion}	energy entrained in ions
E_z	electric field in Cartesian $\hat{z}$-direction
f_{bias}	frequency of the biased stage pulsed inductive device
fc	cyclotron frequency
f_{PI},f_{main}	frequency of stage immediately following bias
FRC	field-reversed configuration
hv	radiative energy from (averaged) excited species decay
$\boldsymbol{I}$	current
ICP	inductively coupled plasma
IEF	ion energy fraction
$I_{g,D2}$	gaseous ionization threshold energy for deuterium
$I_{g,H2}$	gaseous ionization threshold energy for hydrogen
$K_{ex,i}$	rate constant for exciteds with the ith species
$K_{iz,i}$	rate constant for ions with the ith species
$K_{rad} \rightarrow A_{eff}$	effective Einstein coefficient
L	characteristic length
M	neutral, ion, and excited species mass
m	electron mass
n_e	electron number density
n_{ex}	excited species number density
P_{abs}	power absorbed by system
PI	pre-ionization
PIC	Particle-In-Cell
R	characteristic radius
r_L	Larmor radius
$t_{1/4}$	time to ¼-cycle of sinusoidally varying magnetic field
T_e	electron temperature
u_B	Bohm velocity
V	characteristic volume
$v_{\boldsymbol{E}\times\boldsymbol{B}}$	guiding center drift velocity due to orthogonal fields
V_s	voltage drop across the sheath
v_y,v_z	Cartesian velocity components in the $\hat{y}$, and $\hat{z}$-directions, respectively
Δt	pulse duration
ε_{ex}	excitation energy
ε_i	activation energy of the i^{th} species
λ_i	ion-neutral mean free path
ν_m	electron-atom collision frequency
σ_{dc}	DC approximated plasma conductivity
σ_p	AC plasma conductivity

1. INTRODUCTION

Pulsed inductively coupled plasmas (ICPs) have shown potential in multiple disciplines across a variety of operating conditions over the past twenty to thirty years. Applications ranging from microfinish surface etching (100's W up to 100 kW, 100's kHz-10's MHz) [1,2], to space propulsion concepts for long duration in both near-earth and interplanetary missions (10's-100's kW, potentially scalable to MW's, 100's kHz) [3,4,5], to alternative fuel deposition methods in state-of-the-art nuclear fusion research (1's kW-10's MW, 10's-100's kHz) [6,7,8] have all cited an increased need for high performance induction plasmas. The most appealing aspect by far of pulsed ICPs over more conventional ionization techniques is a lack of electrodes and hence a break from the concern over electrode erosion. Common practice is, in fact, to isolate the induction coil from the plasma discharge chamber via a dielectric barrier such as glass, quartz, or high-grade polymer [9,10]. The driving factor for continued research into these devices has been the desire for increasingly higher density plasmas with minimum input power.

Pulsed ICP accelerators have seen a great deal of development over the past 2-3 decades in their application to aerospace electric propulsion (EP). A number of these EP concepts have been bench-tested including the Pulsed Inductive Thruster (PIT) developed by NASA and Northrop Grumman [11,12,13], the Plasmoid Thruster Experiment (PTX) researched at the University of Alabama-Huntsville [14], the Electrodeless Lorentz Force (ELF) thruster researched by the University of Washington [15], the Experimental Coaxial Field Reversed Configuration Thruster (XOCOT) researched by AFRL-Edwards Air Force Base and the University of Michigan [9], and the Faraday Accelerator with Radio-frequency-Assisted Discharge (FARAD) and its Conical Theta-Pinch derivative, CTP-FARAD researched at Princeton's Electric Propulsion and Plasma Dynamics Lab

[16] and NASA's Marshall SFC [17], respectively. PIT has been investigated since the early 1980's by NASA and has seen multiple iterations and refinements. The PIT device is generally characterized by a planar coil geometry (coil diameters ranging from 30 to 100 cm) and a formation and acceleration time of 10-20 μs (discharge frequencies of 100's of kHz). The characteristic length of the inductive plasma in PIT is typically around 3 to 5 cm, yielding a length to diameter (L/D) ratio of 0.05 to 0.1. PTX is primarily characterized by the formation of field-reversed configuration (FRC)[18] plasmas with a purely poloidal, self-consistent (i.e., closed loop) magnetic field. Both PTX (length: 7.62 cm, exit diameter: ~4.8 cm, L/D ≈ 1.6) and the ELF thruster (L/D ≈ 1.4) have a reasonable taper to the coil yielding a more conical geometry. This provides an inherent acceleration mechanism for the FRC by way of an asymmetric magnetic field. Also the ELF thruster utilizes a rotating magnetic field (RMF) for plasmoid formation rather than an oscillating (pulsed, theta-pinch) magnetic field which all of the other devices listed here use. XOCOT (length: 30.7 cm, diameter: 43.5 cm) has an added coaxial inner coil (diameter: 15.8 cm) that assists in stabilizing the formation and compression processes. Typical discharge frequencies of coaxial devices are an order of magnitude slower (discharge frequencies of 10's of kHz), ideally providing longer plasma refinement times and higher ionization fractions. Early models of the FARAD are similar to PIT designs with reference to a planar geometry and method of discharge, while the later CTP-FARAD switches to a conical geometry necessitated by the need to keep puffed (and then pre-ionized) gases closer to the coil face. However the form of propellant injection in both FARAD and CTP-FARAD are substantially modified from PIT to allow for a pre-ionization (PI) stage to increase ionization fraction and thrust

output. This PI stage also allows FARAD to operate at much lower voltages during its main induction phase.

1.1. PULSED DEVICE PRE-IONIZATION

Pre-ionization of propellant gas can be a beneficial addition to the operation of a pulsed ICP accelerator. Early FRC fusion studies showed that insufficient PI can lead to higher resistivity in plasma formations (which corresponds to a reduced plasma temperature) increasing instabilities and reducing fusion energy production [6,19]. Resistivity was able to be reduced by 45% when selective control of the timing and energy levels of the PI stage was enforced. Studies on the XOCOT showed that sufficient PI was imperative for forming a plasmoid [9,20]. More recently, results from the XOCOT-T have shown that a pre- pre-ionization, or pre-PI, glow-discharge can aid formation. Finally, results from the FARAD device have shown that an RF stage PI just before a primary discharge can lower the required discharge voltage for forming and accelerating the high-density current sheet produced by a pulsed ICP accelerator. It was reported however, that little difference in performance was seen for RF PI operating powers ranging from 500 to 1000 watts. While PI and pre-PI are known to affect the overall performance and operation of pulsed ICP accelerators, these results and others emphasize the gap in research focused on how to best implement or operate these pre-ionization stages.

Section 2 describes a numerical approach to a parametric study of an RF plasma source in the context of pre-ionization. The pulsed inductive RF plasma is envisioned as a PI source for a pulsed ICP accelerator and results from simulations are analyzed from this perspective. Metrics of specific interest here are the ion energy fraction and plasma conductivity. The ion energy fraction is formally defined in Section 2.3.1, however a

loose definition is the fraction of total input energy entrained in ions. These metrics are analyzed assuming the RF PI is immediately followed by a higher energy pre-ionization or a main discharge. We investigate how variation of PI RF source characteristics, such as pulse duration and total energy, affect these subsequent processes. Additionally, a constant power analysis is performed by matching values of pulse duration and energy addition. First, a brief description of the global model used is presented with deferment of further detail and model verification to previous works. Next, results and trends are highlighted. Finally, analyses of results and their relevance to pulsed ICP devices is made with an emphasis towards fixed-power space propulsion applications.

1.2. PULSED THETA-PINCH DEVICES

The theta-pinch concept is one of the most widely used pulsed inductive plasma source designs ever developed. It has established a workhorse reputation within many research circles including; thin films and material surface processing [21,22,23], fusion [24,25,26], high-power space propulsion [27,28], and academia [29,30], at times filling the role of not only a simple plasma source but also that of a key component in a larger test article. In super-conductive thin films, theta-pinch ionization has been used as an electrode-less alternative ion injection source. Recently, the University of Illinois at Urbana-Champiagn has developed the Divertor Erosion and Vapor Shielding eXperiment (DEVeX), a theta-pinch plasma source to study vapor shielding of lithium surfaces exposed to plasmas. Several theta-pinch schemes have been used worldwide since the 1970s to form field-reversed configuration (FRC) plasmoids for use in fusion proof-of-concept studies and experiments [31,32]. In recent years, interest in future high-power space electric propulsion (EP) concepts involving the formation and acceleration of heavy gas (i.e., Ar, Xe, etc) FRCs via theta-pinch coils has grown in both the public and

private sector [33,34]. Despite a long history of research and utilization, initial onset ionization mechanisms in theta-pinch plasmas often go overlooked or under-appreciated due to either a primary interest in the quasi-steady state conditions (in films and materials surface processing and academia), insufficiently high acquisition rates ($\Delta t < 10^{-7}$-10^{-8} s) diagnostics (in fusion and propulsion studies), or a larger interest in the high energy, high density final state of the plasma (in fusion and materials processing).

Theta-pinch devices utilize a relatively simple coil geometry to induce electromagnetic fields and create plasma. A typical theta-pinch coil consists of a single-turn that wraps cylindrically around a gas while current, ***I***, flows in an azimuthal direction (see Figure 1.1). Ignoring end effects, this current induces a uniform axial magnetic field, ***B***. Often an initial bias magnetic field is applied, opposite in axial orientation to latter stages, by a quasi-steady current (steady with respect to subsequent discharges, f_{bias} ≈ 1's to 10's of kHz) which has been shown over several studies to improve formation by way of either plasma "preheating" or increasing trapped magnetic flux [35,36,37,38]. When axial magnetic field is changing in time (i.e., $d\boldsymbol{I}/dt \neq 0$) it induces an electric field, ***E***, described by Faraday's law (stated by equation (14) for reference) that opposes the changing current. This process is illustrated in Figure 1.1 which shows a cut-away of typical theta-pinch operation during an initial current rise.

$$\text{Faraday's Law;} \quad \oint \vec{E}\cdot\vec{dl} = \frac{-d}{dt}\int \vec{B}\cdot\vec{dA} \tag{1}$$

The current rise (and subsequent ringing time-domain profile) is essentially the result of a typically under-damped LRC circuit where the coil represents the principal inductance (L) and is driven by a high voltage (10's to 100's of kV) capacitor bank (C). Some theta-pinch test articles utilize multiple discharge stages with the first post-bias discharge

commonly referred to as pre-ionization. Pre-ionization (PI) stages are typically characterized by lower energies at higher frequencies relative to main discharges (i.e., $f_{PI} > f_{main} >> f_{bias}$). Typical theta-pinch ringing discharge frequencies range from 100's of kHz to 10's of MHz depending on the stage. While implementation of bias fields have become commonplace in theta-pinch devices for fusion and EP studies they remain a point of contention in terms of how best to implement them and ultimately whether or not they are as useful (i.e., necessary) as reported in literature.

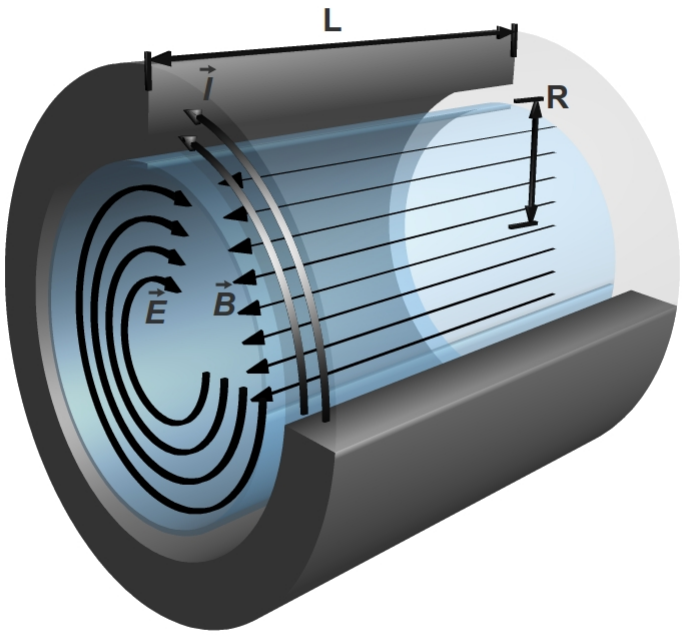

Figure 1.1: Ideal theta-pinch field topology for an increasing current, *I*.

Early work on the Scylla I theta-pinch device during the 1960's at Los Alamos National Laboratory (LANL) by Little *et al* demonstrated that "both strong pre-ionization and a bias field B_0 antiparallel to the main compression field B_z are necessary to produce neutrons during the first half-cycle of the discharge."[35] The Scylla I device produced bias and main discharge fields of 0.4 and 5.5 T, respectively. Also in 1966 experiments on the Megajoule Theta-Pinch at the Culham Laboratory in the U.K. by Green and

Newton attempted to provide explanation for losses in trapped bias flux when bias field is sufficiently high ($B_{bias} \approx 300$ mT) [39]. Authors of that work proposed that a portion of the initial bias flux is lost almost immediately when applied magnetic field passes through zero (onset by field reversal). Plasma would rebound and briefly come into contact with the walls, neutralizing electrons and releasing the portion of magnetic field retained by these electrons. Experimental results reported during the 1980's on the Field Reversed eXperiements (FRX-A,B) by Armstrong *et al* also at LANL highlighted the significance of the bias magnetic field nullification (referred therein as net magnetic field zero-crossing) by the ringing theta-pinch field profile in providing high levels of ionization [24,36,40]. Bias and PI field magnitudes were reported to be 70 and 110 mT, respectively, for FRX-A and 230 mT for both in FRX-B. However the FRX-A,B reports appear to have provided only observations without explanation for why this zero-crossing is critical.

Since around the turn of the 21st century collaborative efforts between the Air Force Research Laboratory (AFRL) and LANL have focused on the use of FRCs to demonstrate feasible, very high temperature, high density mass delivery systems for fusion and high energy density plasma research [25,26,41,42]. First from around 2000 to 2007 with the Field Reversed eXperiment – w/Liner (FRX-L) at LANL and then in 2007 constructing the Field Reversed Configuration Heating eXperiment (FRCHX) at AFRL-Kirtland, these proof-of-concept studies seek to conduct FRC capture and compression with the goals of demonstrating magnetized target fusion (MTF) and studying the high energy density plasma state. As with earlier results, ionization is reported to form when the bias field has been approximately nullified (see Figure 1.2) by the first ring of the theta-pinch PI field, when *dB/dt* approaches zero (i.e., when electric field is at its

weakest) [41]. While the earlier recommendations of Armstrong *et al* suggest to incorporate this zero-crossing, for the FRCHX experiments this leads to an initial plasma formation with little to no trapped magnetic flux which in turn reduces FRC lifetime. In addition, the FRCHX results seem to contradict what an *electrostatic* approach for ionization would predict, which is that the greatest levels of ionization would occur when the electric field is first peaked (i.e., when the theta-pinch PI is initially triggered). At present there is no explanation for what is occurring during this early time and why there is a delay in plasma formation to the net field zero-crossing.

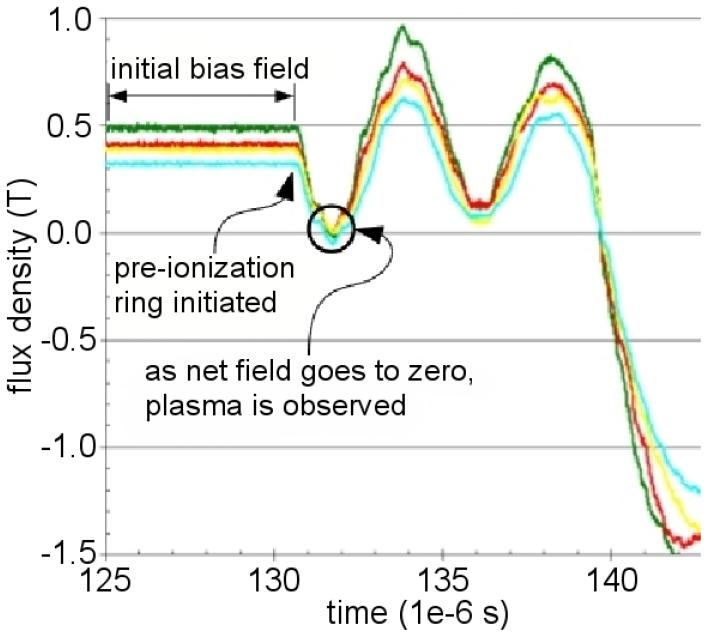

Figure 1.2: Reported magnetic field results (integrated B-dot probe data) from FRCHX (Ref 41).

The research presented in this article provides explanation for some of these on-going observations. To gain insight into the fundamental kinetic effects that bias field introduces in a theta-pinch device, interpreted magnetic and electric fields and geometry from FRCHX are used as test case data for both an analytical single electron and particle-in-cell study. These insights are meant to elucidate the electron kinetics during onset of

the breakdown processes when a bias field is present. First the essential problem statement is described along with assumptions (and justifications therein) used in this approach. Second, baseline results from a single electron study as well as a particle-in-cell study for verification are presented along with highlights of the parallels with FRCHX results. Third, parametric analysis of the electron energy involving bias field offset and post-bias field amplitude is presented with qualitative comparison to past theta-pinch experiments. Finally conclusions are drawn assessing the impact of these results on theta-pinch operation in general.

2. PARAMETRIC STUDY OF RF PRE-IONIZATION OPERATION

2.1. MODEL DESCRIPTION

Modeling of inductive plasmas has met reasonable success with the primary goal of predicting plasma characteristics at the end of the induction phase to optimize efficiencies. Some have used numerical simulation to show theoretically that modulation of the induction profile can result in reduced ion production cost, higher ionization fraction, and increased plasma lifetime [1,43,44]. Others have used numerical analysis to study and optimize the induction phase of pulsed ICP accelerators [45,46]. Our approach is to slightly modify an existing, well-documented pulsed inductive RF plasma model and use it to study how PI source characteristics affect parameters that are important for a pulsed inductive accelerator, such as ion energy fraction and optimum pulse timing. Therefore, an already-published, globally-averaged, time-resolved model is reproduced from Ashida *et al* [47] and modified for our problem statement. This model is derived from the methods outlined for steady state systems [48,49] and review of these and other techniques is also summarized in literature [50]. Developed with a focus on argon gas (monatomic gas) this methodology proves comparatively simple against more computationally intensive particle-in-cell, MHD, or hybrid simulation codes. A brief description of the system of equations used by this model follows, while a more detailed model description along with verification studies against original reported results has been presented previously by the authors [51]. The results of the verification study can be seen in Figures 2.1a-c and 2.2a-c. Figure 2.1 is directly taken from Ref. [47] while Figure 2.2 is results produced from the code presented in APPENDIX A.

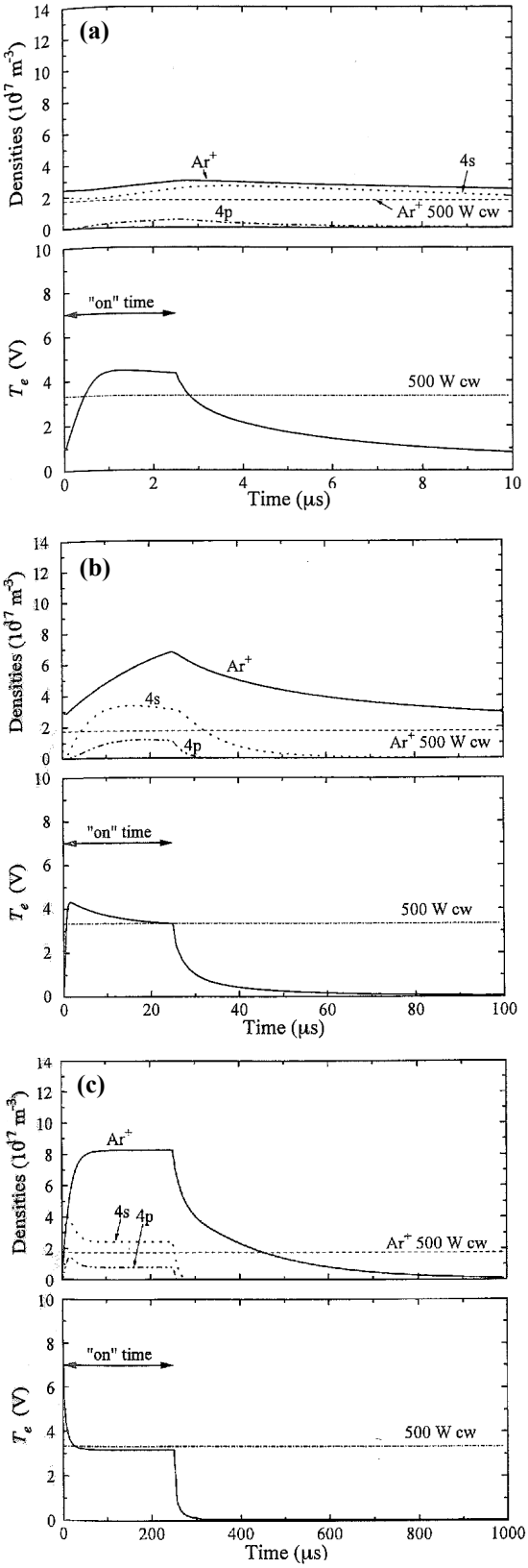

Figure 2.1: Reported results for 100 kHz, 10 kHz, and 1 kHz; 2000 W at 25% duty cycle from Ref [47].

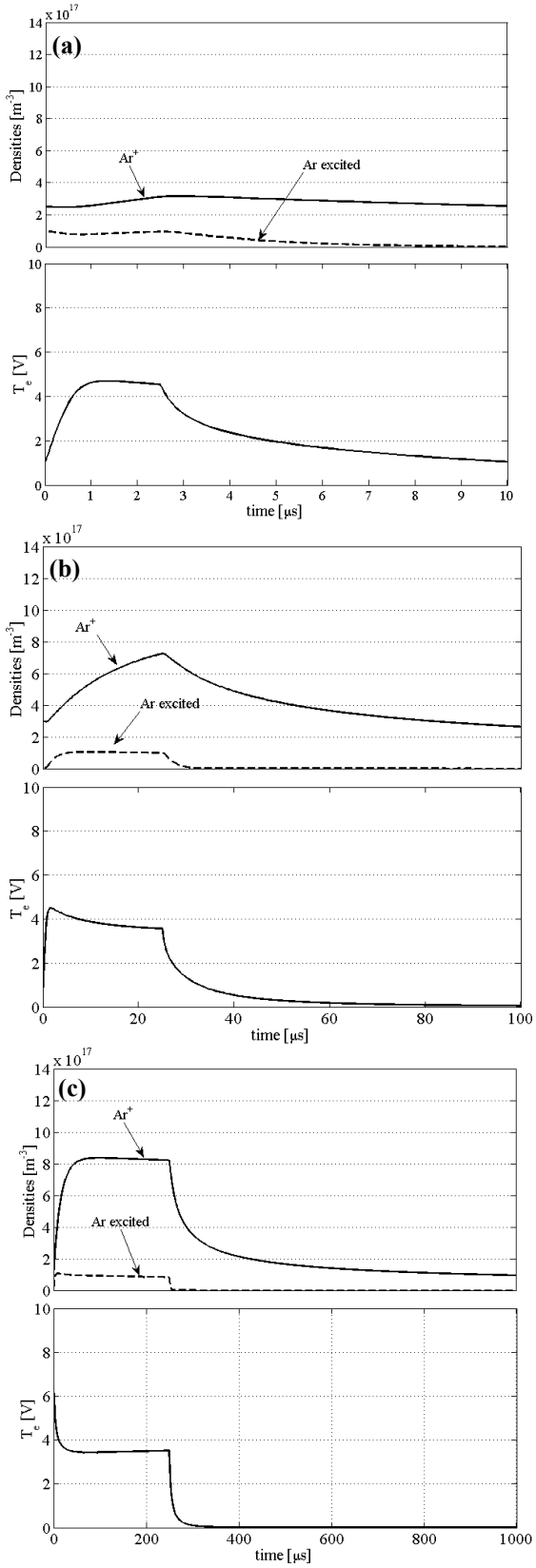

Figure 2.2: Reproduced results of the same with single averaged excited species (work presented here).

Notice that the original work described two specific excited states for Ar I; the 4s and 4p levels. Comparison of each case from Ashida *et al* with that of the work presented here provides good agreement and thus it is concluded by the author that sufficient reproduction of the original model has occurred.

For the analysis of focus here the original published model is reduced from four coupled rate equations to three by dropping the two separate excited states in favor of a single average excited state with excitation energy, ε_{ex}, of 12.14 volts. Rate constants for this average excited state are taken from Lieberman and Lichtenberg [52]. The excited state rate equation is then given by (2), which includes electron-neutral collision rates, spontaneous decay to ground, and diffusion losses to the walls of a thin sheath cylinder.

$$\frac{dn_{ex}}{dt} = \sum_i K_{ex,i}\, n_e\, n_i - K_{rad}\, n_{ex} - D_{eff}\, n_{ex} \left[\left(\frac{\pi}{L} \right)^2 + \left(\frac{2.405}{R} \right)^2 \right] \tag{2}$$

L and R are the length and radius of a characteristic cylindrical geometry (taken to be 7.5 cm and 15.25 cm, respectively, or L/D ≈ 0.25 from Ashida *et al* [47]) and D_{eff} is an effective diffusion coefficient calculated for a gas pressure and temperature of 5 mTorr and 600 K, respectively. These values of pressure and temperature remain consistent throughout all studies presented here. It's also noted that the length to diameter ratio referenced and used in this model and throughout the following studies falls into the range highlighted in section 1 (i.e., 0.1-1.6) for pulsed ICP accelerators used in EP, in addition to being similar to those commonly used in pulsed ICP experiments of other disciplines. Also, K_{rad} is taken to be a reduced effective Einstein coefficient, A_{eff}, as outlined in the appendix of Ashida *et al* [47]. Balance of electrons is given by (3) which includes ionization and recombination as well as losses to the walls.

$$V\frac{dn_e}{dt}=V\sum_i K_{iz,i}\,n_e\,n_i-n_e\,u_B\,\Lambda_{sheath} \tag{3}$$

where,

$$\Lambda_{sheath}=\frac{0.86\left(2\pi R^2\right)}{\sqrt{3+\frac{L}{2\lambda_i}}}+\frac{0.80\left(2\pi R L\right)}{\sqrt{4+\frac{R}{\lambda_i}}} \tag{4}$$

Then, imposing a quasi-neutral assumption, rate of change of ions is also given by (3). Sheath losses to the walls in (4) is estimated by the original authors from analytical solutions presented by Godyak and Maximov for diffusion at the sheath edge. Volume, V, of the plasma also assumes a thin sheath meaning $V=\pi R^2 L$ and λ_i is the ion-neutral collision mean free path calculated by a Maxwellian electron distribution averaged over argon ionization cross-section data [53]. Assuming free diffusion of neutrals is negligible during the time-scales of interest (i.e., cold neutrals with no direct losses), then an additional, dependent rate for neutral species can be constructed from rate constants involving the excited and electron species.

Energy balance is achieved through equating total power absorbed from the pulsed device to the plasma (assumed known) to all loss and energy transfer mechanisms. Namely, species creation/destruction, loss to the walls, and overall electron temperature increases.

$$P_{\text{abs}}(t)=V\left[\frac{d}{dt}\left(\frac{3}{2}e\,n_e\,T_e\right)+e\,n_e\sum_i \varepsilon_i K_i\,n_j\right]+n_e\,u_B\,\Lambda_{sheath}\left(e\,V_S+\frac{5}{2}e\,T_e\right)=\frac{dE_{\text{abs}}}{dt} \tag{5}$$

where P_{abs} is the total power input to the system as a function of time, ε_i and K_i are the energy and reaction rate constant, respectively, associated with the i^{th} reaction, n_j is the non-electron species involved in the reaction, Voltage drop across the sheath, V_S, is given by

$$V_S = \frac{T_e}{2} \ln\left(\frac{M}{2\pi m}\right) \quad . \tag{6}$$

where *M/m* is the ion-electron mass ratio. Known power absorbed is input via a positive-bias, square-wave pulse. The time derivative term in (5) involving n_e and T_e is separated by the product rule and the set of differential equations (2), (3), and (5) are solved simultaneously. Rate constants used the above formulations are listed in Table 2.1.

Table 2.1: Rate Constants for all reactions used in the modified model presented here.

Reaction	*Rate constant, K_i (m^3/s)*
Ar+e (elastic) [a]	$2.336\times10^{-14}\ T_e^{1.609} \exp[0.0618\ (\ln T_e)^2 - 0.1171\ (\ln T_e)^3]$
$Ar+e \rightarrow Ar^*+e$ [a]	$2.48\times10^{-14}\ T_e^{0.33} \exp[-12.78/T_e]$
$Ar^*+e \rightarrow Ar+e$ [b]	$6.88\times10^{-16}\ T_e^{0.33}$
$Ar+e \rightarrow Ar^++2e$	$2.3\times10^{-14}\ T_e^{0.68} \exp[-15.76/T_e]$
$Ar^*+e \rightarrow Ar^++2e$	$9.34\times10^{-14}\ T_e^{0.64} \exp[-3.40/T_e]$
Reaction	*Einstein Coefficient, A_i (s^{-1})*
$Ar^* \rightarrow Ar+h\nu$ [c]	$A_{eff} \approx 5.14\times10^5$

[a] *Source from Lieberman and Lichtenberg* [52] *valid in the range 1 to 7 eV.*

[b] *Estimated by detailed-balance analysis.*

[c] *Reduced effective decay rate outlined in appendix of Ashida, Lee, and Lieberman* [47]

2.2. RESULTS

Simulations are performed for varying applied energy pulse duration and total applied energy. Fixed energy over a fixed duration provides the specific (time average) power level of an RF source which can be easily tuned by adjustment of circuit parameters and antenna geometry or in many cases is directly tunable on an amplified frequency generator. To provide initial *"seed"* electron density, high voltage DC electrodes are typically introduced far up-stream of the pulsed ICP accelerator induction

chamber and their output is directly proportional to the voltage applied. In the results that follow for varied pulse duration and energy initial densities of 8×10^{19}, 1×10^{17}, and 2.5×10^{17} m^{-3} are used for the ground, excited, and ion/electron species, respectively. Later constant power studies use a seed electron/ion density of 10^{15} m^{-3} for reasons cited in that section. In all studies presented here a constant gas pressure and temperature of 5 mTorr and 600 K, respectively, along with dimensions identical to the Ashida *et al* modeling (L/D ≈ 0.25 as stated above) are assumed. Total absorbed energy is not directly controlled, but represents a measure of the overall power scalability of the pulsed ICP accelerator device.

For all of the following studies the earlier stated geometry is used and further description of these different test cases and simulation results are provided in the following sections.

2.2.1. Variance in Pulse Duration. Variation of pulsed power duration is investigated while keeping total energy input constant. This approach yields an increase in time average power for decreases in duration time. The baseline simulation is derived from the 100 kHz case of Ashida *et al* [47]. This consisted of a total energy deposited, initial electron temperature, and neutral gas temperature of 5 mJ, 1 eV, and 600 K, respectively. Pulse duration, Δt, is varied based on an exponential decay of the total observation time of 5 μs represented by

$$\Delta t = \frac{5\times10^{-6}}{1.5^{n}} \text{ (s)}. \tag{7}$$

This scheme yields durations of 3.33×10^{-6}, 2.22×10^{-6}, …, 1.14×10^{-8} seconds for n=1, 2, …, 15. Because total energy deposited (5 mJ) is constant, as pulse duration

decreases, power increases accordingly. Figure 2.3 shows the density and electron temperature results for pulse durations of 3.33×10^{-6} seconds and 1.14×10^{-8} seconds. These were the longest and shortest pulse durations tested. For the shortest pulse duration, ion density initially increases reaching a peak of 3.7×10^{17} m^{-3} at 0.8 μs and then decreases. The longest pulse duration ion density slowly ramps up, achieving a peak of 3.1×10^{17} m^{-3} at 3.6 μs. Despite these different trends, by the end of 5 μs densities for the two runs fall to within approximately 12% with the shorter pulse duration having higher density. Electron temperature initially increases and then decreases for both pulse durations. However, the temporal profiles are very different. Electron temperature for the shortest pulse duration increases quickly to 15.6 eV in about 0.01 μs and then quickly decays to less than 4 eV at 0.8 μs. Electron temperature for the longest pulse duration ramps up more slowly, reaching 4.2 eV at 1.0 μs and then remaining relatively constant at 4.3 eV from 1.1 to 3.3 μs before slowly decaying. At a time of 5 μs, final electron temperature for the short duration case is 35.5% less (at 1.43 eV) than that of the long duration case (at 2.22 eV).

The differences in the electron temperature and ion density profiles of Figure 2.3 are due to the input power, or the time over which energy is added to the plasma. When energy is added to the electrons very quickly (shortest pulse duration), electron temperature spikes and then decays as ionization and wall losses cool the electron population. This concept of T_e overshoot resulting from a limited number of available electrons at early times is not a new phenomenon and has been observed by others in both experiment and simulation [43,54,55,56]. High electron temperature at early time results in more energetic collisions and thus ion density also peaks early. When the energy is

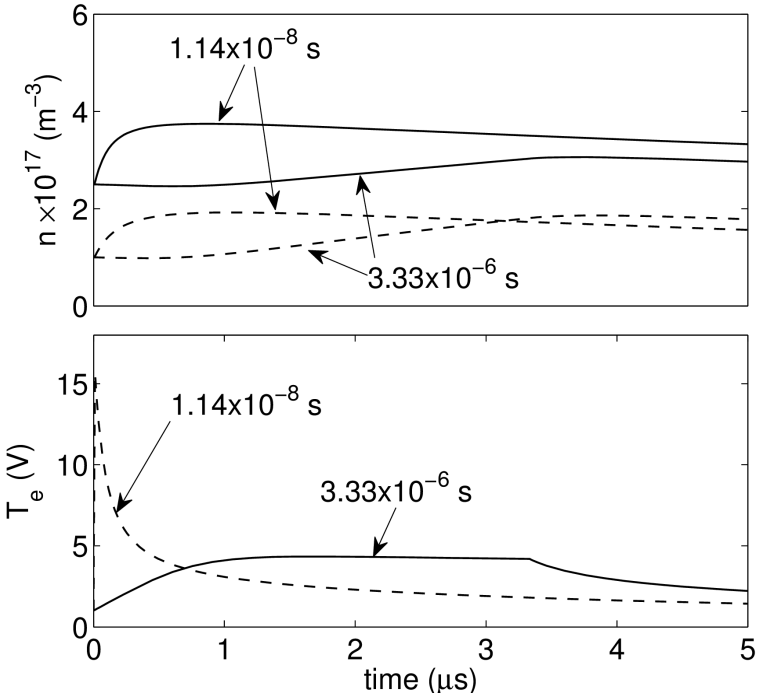

Figure 2.3: Results for variation of pulse duration highlighting electron temperature over-shoot. Solid and dashed lines represent ionized and excited species, respectively, in density plot.

added slowly (longest pulse duration), electron temperature slowly increases and then reaches a plateau. This plateau is indicative of equilibrium, where energy is being added to the electron population at the same rate it is removed. Over this time interval the ion density slowly grows.

The discontinuity in the electron temperature at 3.33 μs corresponds with the end of the energy addition pulse. When energy addition ends, the electron population cools, usually very abruptly.

2.2.2. Variance in Total Energy Deposition. Variation of total input energy is also investigated. This approach holds pulse duration constant and thereby also increases time average power to the system. All initial quantities stated for the varied duration case above are also used here minus the fixed energy of 5 mJ. Energy absorbed, E_{abs}, is initially set at 5.0 mJ and exponentially increased via

$$E_{\text{abs}} = 5 \cdot \left(2^{n}\right) \text{ (mJ)} \tag{8}$$

yielding total input energies of 5, 10, …, 160 mJ for n=1, 2, …, 6. Figure 2.4 shows the variation of densities and electron temperature for two cases, the 5 mJ (low energy) and 160 mJ (high energy) cases. Ion density in the high energy case can be seen to have a much higher rise rate in the early times (0 to 2 μs) at approximately 24.4×10^{17} m^{-3} μs^{-1} compared to 0.40×10^{17} m^{-3} μs^{-1} for the low energy case. When the power input shuts off at 2.2 μs, ion levels remain constant for the remainder of the simulation, while excited states begin to show noticeable decay. This is recognized as a result of the difference between species lifetimes as governed by the rate constants. Particularly the spontaneous decay rate for excited state argon represents a substantial loss mechanism for excited species. Peak ion and excited densities for the low energy case are 3.2×10^{17} and 1.9×10^{17} m^{-3}, respectively, and occur at 2.6 and 2.8 μs, respectively. Peak ion and excited densities for the high energy case are 6.6×10^{18} and 1.8×10^{18} m^{-3}, respectively, and occur at 3.9 and 2.2 μs, respectively. These peak times occur just past the power-off time of 2.22 μs except for the high energy ion case which is 1.6 μs past power-off. In the lower plot of electron temperature the low energy case peaks to 4.8 eV at 1.16 μs and the high energy case at 16.2 eV at 0.13 μs. As before a T_e overshoot is seen for the high energy case. Despite large differences in initial trends, final electron temperature between the two cases is within about 9% at the end of the simulation at 5 μs, with the high energy case (1.7 eV) just below the low energy case (1.8 eV). It should be noted here that, similar to above results, final ion densities are very different (~95%), while final electron temperature is nearly identical.

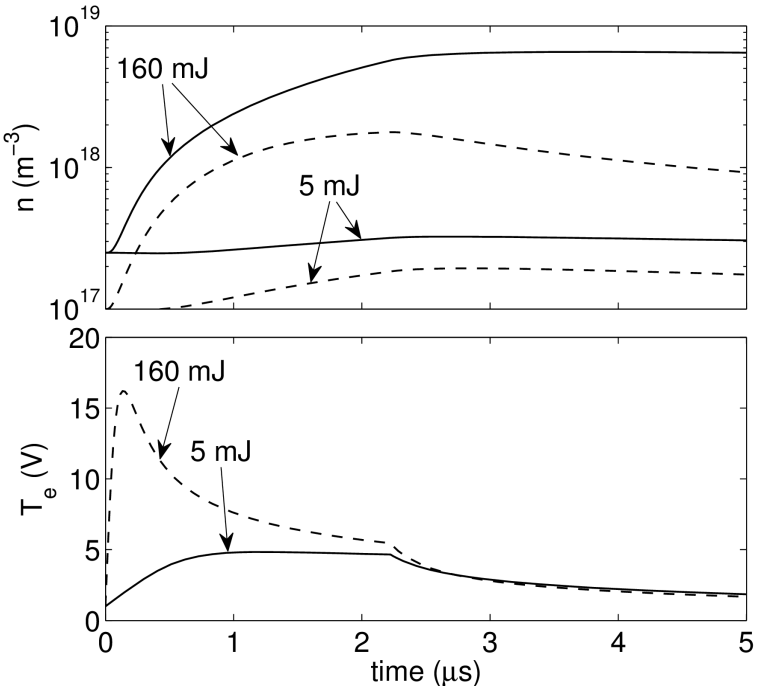

Figure 2.4: Results of variation in total energy deposition highlighting the 5 mJ and 160 mJ cases. Solid and dashed lines represent ionized and excited species, respectively, in density plot.

2.3. ANALYSIS AND DISCUSSION

An analysis and discussion of plasma simulation results is presented in this section. Specifically, results are analyzed from the perspective of an EP propulsion system, assuming the pulsed inductive RF plasma is functioning as the pre-PI stage for a pulsed inductive accelerator stage. In general, desirable PI plasma has low ion production cost and high density, as well as sufficient conductivity for good coupling during the main induction phase.

First a description and rationale for the metrics used in analysis are described. Then these metrics are used to analyze PI source characteristics of pulse duration, total energy deposition, and time average power.

2.3.1. Detail of Analysis Metrics. A desirable PI plasma has a low ion production cost and provides a high level of inductive coupling. To evaluate results of the above studies against these criteria, analysis metrics used in the following discussion are peak ion energy fraction and electron-neutral conductivity. It can be shown that electron-neutral collisions are dominant at the densities (i.e., pressures) tested of 10^{17} m^{-3}, and because the plasma is weakly ionized (<10%). Thus, we focus here on electron-neutral driven conductivity.

For a given EP system input electric power, P_{elec}, a power balance analysis of the device yields,

$$P_{elec}\,dt = E_T + E_{ion} + E_{rad} + E_{loss} + E_{therm} \tag{9}$$

where E_T, E_{ion}, E_{rad}, E_{loss}, and E_{therm} are the energy totals partitioned out to thrust, ionization, radiation, other loss mechanisms, and overall heating of the gas, respectively. Efficient thruster design drives the necessity for E_T to be large relative to all other terms, while still recognizing the necessity for E_{therm} and E_{ion} to produce the plasma that is accelerated. However, E_{ion}, E_{rad}, E_{loss}, and E_{therm} should all be minimized for a given accelerated plasma plume density to reflect a low ion production cost.

Input energy absorbed in a PI plasma, E_{abs}, heats the gas, produces ions, and is lost via radiation and diffusion to the walls. This can be expressed as

$$E_{abs} = E_{ion} + E_{rad} + E_{walls} + E_{therm} = P_{abs}\,dt\ . \tag{10}$$

As the plasma evolves over time energy is converted between these different forms. For instance, energy is initially deposited into thermal electron energy, where it is used to produce ions and excited species. Energy is then lost when excited species radiatively

decay and ions and electrons diffuse to the wall. To achieve the lowest ion production cost and maximize the effectiveness of an RF source, the PI plasma should be passed on to main induction when the instantaneous *ion energy fraction* (IEF) is highest. This fraction is defined here as

$$ion\,energy\ fraction \stackrel{\text{def}}{=} \frac{E_{ion}}{E_{abs}} = \frac{V\left(n_{ion} - n_{ion0}\right) e\,\varepsilon_{iz}}{\int_t P_{abs}\,dt} \tag{11}$$

where n_{ion0} is the initial density of ions governed by the level of seed plasma used. The density difference in (11) ensures that only the energy entrained in newly created ions is accounted for. It is emphasized that the denominator of (11) equals the total power absorbed up to time t. This is key to the information this ratio conveys because it includes not only the energy tied to the charged and excited species but also any and all forms of energy loss up (within the models abilities) through time t. Peak IEF is the first of two metrics used for analysis here.

Immediately following the pre-PI stage of a pulsed ICP accelerator is either a PI or main discharge stage. To maximize inductive coupling of these typically higher power discharges with the plasma, a highly conductive (or alternatively, a minimally resistive) plasma exit-state from the RF pre-PI is necessary. In other words, the conductivity of the plasma at the *end* of the pre-PI RF stage is of primary importance and, as such, conductivity should be evaluated based on frequencies seen in these subsequent discharge stages. It is this rationale that permits a DC approximation since PI and main discharges are typically of a much lower frequency than observed plasma collisional frequencies (i.e., $w << \nu_m$). This yields a conductivity of

$$\sigma_p \rightarrow \sigma_{dc} = \frac{e^2 n_e}{m \nu_m}\ . \tag{12}$$

Keeping in mind that electron-neutral collision frequency increases with increased electron temperature, it can be seen from (12) that a cool, dense plasma is desired to maximize conductivity and hence maximize inductive coupling. In the following sections the metrics of peak IEF and peak DC plasma conductivity are used to evaluate the characteristics of the RF pre-PI plasma source.

2.3.2. Pulse Duration. Time evolution of IEF is shown in Figure 2.5 for the longest pulse duration as well as six lower durations down to 0.3 μs. At early times, IEF falls below zero as a result of plasma density dropping below initial seed density before collisions are able to dominate at increased electron temperatures, introducing a negative value in the density difference, n_{ion}-n_{ion0}, seen in (11). For the long duration of 3.3 μs ion density initially drops below seed density due to wall losses before returning to, and surpassing seed density levels just after 1.0 μs. The long duration case then peaks at 15.5% at 3.77 μs before decreasing to a final value of 13%. As duration is decreased the initial density drop is mitigated more quickly and peak fraction is seen to increase and occur at subsequently earlier times. This trend agrees qualitatively with that of electron temperature for reduced pulse durations as shown in Figure 2.3. Reducing pulse duration by an order of magnitude (3.3 μs to 0.3 μs) shows a greatly increased peak energy fraction of 32.3% at 1.0 μs before then decreasing in a linear trend to a final value of 21%.

Peak IEF is plotted in Figure 2.6 and shows that IEF more than doubles from longest to shortest pulse duration. Specifically, 15.5% and 34.4% for the longest and shortest pulse durations, respectively. IEF remains high (33.5%) out to 1.3×10^{-7} seconds, then decreases. Put another way, analysis of Figure 2.6 shows that for all other

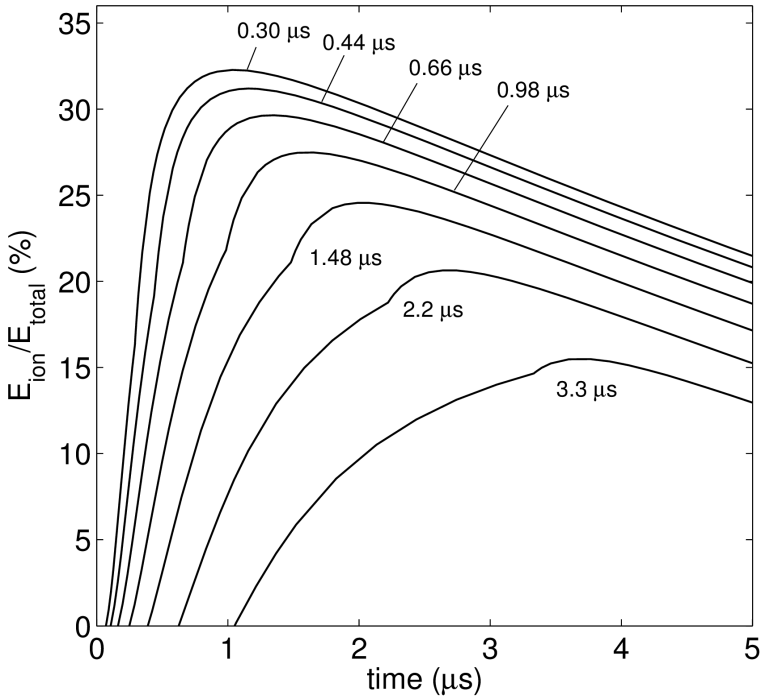

Figure 2.5: Ion energy fraction (IEF) over time from longest pulse duration (3.3 µs) to a factor of 10 reduction (0.3 µs).

conditions being equal, reducing pulse duration time by a factor of 10 (from 10^{-6} to 10^{-7} seconds) yields a gain of only 16.5% of input energy stored in ions. Decreasing duration time further (from 10^{-7} to 10^{-8} seconds) yields an additional 2.5% increase in IEF.

Timing is critical in any pulsed power application, especially in inductive plasma thrusters. When varying the delay between pre-ionization and a main induction phase, delays on the order of µs have shown significant differences in plasma formation (and, by extension, thruster performance). So then, not only is a higher IEF important but the time at which that peak ratio occurs is also important because this is the optimum time to eject the plasma (i.e. when the device has reached the most ions for the least energy lost). To investigate this further, the time at which the peak IEF is reached is also plotted in Figure 2.6. Some slight discontinuities in this plot can be seen which are a result of finite

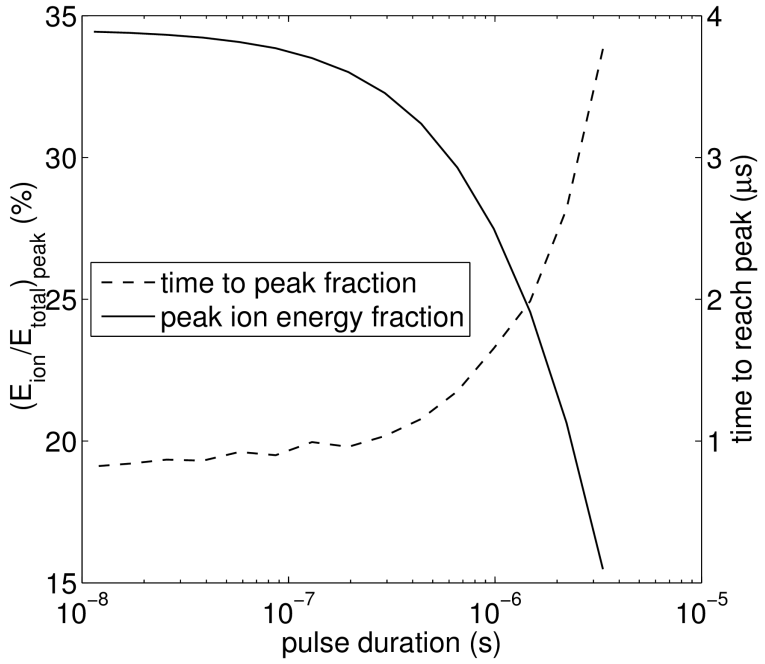

Figure 2.6: Peak IEF and time to reach peak for varied pulse durations.

convergence tolerances in the iterative differential equations solver. Figure 2.6 shows that for a reduction in pulse duration from 3×10^{-6} to 3×10^{-7} the optimum firing time is reduced from just over 3.5 μs to just over 1 μs. Additionally, Figure 2.6 shows that pulse durations below 2×10^{-7} seconds (about 200 nanoseconds) yield little benefit.

Figure 2.7 shows conductivity profiles over time for pulse durations tested. Conductivity for the longest duration (3.3×10^{-6} s) is shown along with six consecutively shorter durations down to a pulse reduced by approximately a factor of 10 (0.3×10^{-6} s). Conductivity starts at around 3.8 $m\Omega^{-1}$ m^{-1} for all pulse durations as governed by identical initial electron temperature and seed density. This initial conductivity proves to be higher than final conductivity for all duration cases. It should be noted however, that this is misleading because at early times collision frequency is very small which drives σ_{dc} large despite the plasma density being at it's lowest. Subsequently, this early phenomenon is

ignored for the analyses presented here. For the long pulse duration of 3.3 μs conductivity initially decreases at a decay rate of about 1.1 $m\Omega^{-1}$ m^{-1} per μs during the first 0.3 μs until leveling off to a minimum of 0.45 $m\Omega^{-1}$ m^{-1} at 1.2 μs. A steady increase follows up to a final value of 1.3 $m\Omega^{-1}$ m^{-1}. Conductivity profile for the 90% reduced pulse duration (0.3×10^{-6} s) shows a much steeper decay rate initially at approximately 58 $m\Omega^{-1}$ m^{-1} per μs approaching a minimum of 0.3 $m\Omega^{-1}$ m^{-1} at 0.18 μs. The short duration conductivity profile then increases, quickly surpassing the long duration final value at 1.8 μs. Final conductivity of the short duration reaches 2.7 $m\Omega^{-1}$ m^{-1}. All conductivity profiles show a rate of increase after power-off time at a rate of approximately 0.45 $m\Omega^{-1}$ m^{-1} per μs.

The above analysis shows that a reduction in pulse duration by a factor of 10 yields an increase in final conductivity of 110%.

2.3.3. Total Energy Deposition. Available energy and power (the rate at which the available energy can be delivered) are the key factors in any space vehicle's capability and mission flexibility. So making the most of that power is critical to device design. In this section several energies, over a wide range of power levels are compared against the results of pulse duration modulation. Figure 2.4 shows that upon increasing input energy by a factor of 32 (5 mJ to 160 mJ) the final ion density increases by a factor of 20 (3×10^{17} to 6×10^{18} m^{-3}). Relating this to Figure 2.6 shows that reduction of the pulse duration, which corresponds to an increase in power (for a set total energy), provides an increase in effective energy usage for ion production.

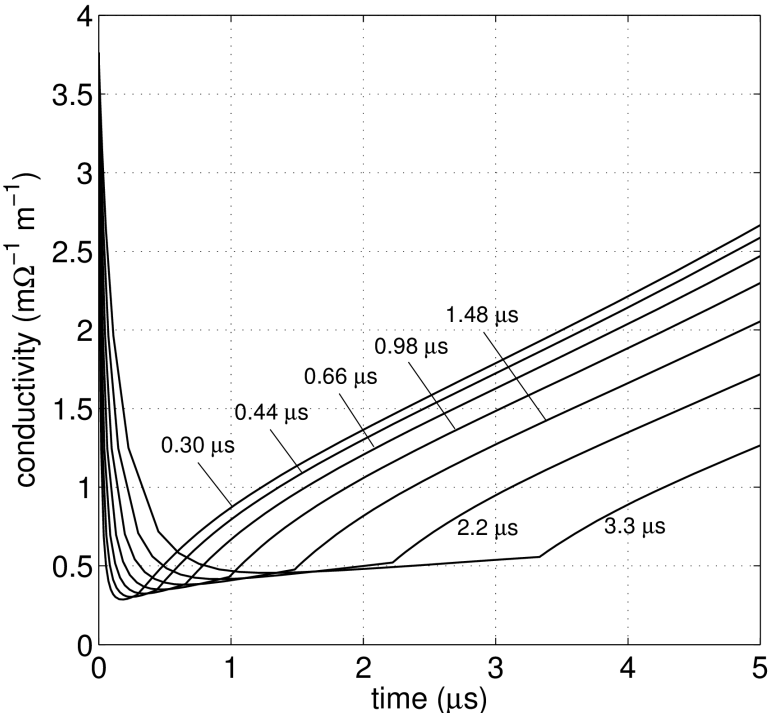

Figure 2.7: Conductivity profiles over time from longest pulse duration (3.3 μs) to a factor of 10 reduction (0.3 μs).

Figure 2.8 shows IEF versus pulse duration for the six energy cases. Here IEF has a shifting peak which moves to longer duration times for higher energies. The 160 mJ case peaks to 58.4% at 2.9×10^{-7} seconds. As input energy increases the decay rate in IEF becomes *less* pronounced. Similar to the above analysis, to illustrate this data points at the two longest pulse durations are once more used to obtain a decay rate. The low energy case of Figure 2.8 exhibits the greatest decay rate at 4.6% μs^{-1}. To clarify, this means that at pulse durations of 10^{-6} and longer, for 5 mJ energy input, the peak IEF is reduced by 4.6% for every μs increase in pulse duration. By contrast, the high energy case is only 2.0% μs^{-1}. Additionally it is noticed that as energy input increases, the peak IEF increases which shows that as larger energies are put into the system more energy is going into ion production than either losses or excited state atoms or both.

Also Figure 2.8 shows that the increase in peak IEF diminishes each time input energy is doubled. Put another way, the peak IEF shows an exponential decay relationship with energy input. It is not clear currently what this limit but appears to be near 60% to 65%. The energy limit of 160 mJ is considered a very high limit because 160 mJ at a pulse duration of 1.14×10^{-8} seconds yields a power level of around 14 MW which is orders of magnitude higher than any current EP spacecraft power plant to date.

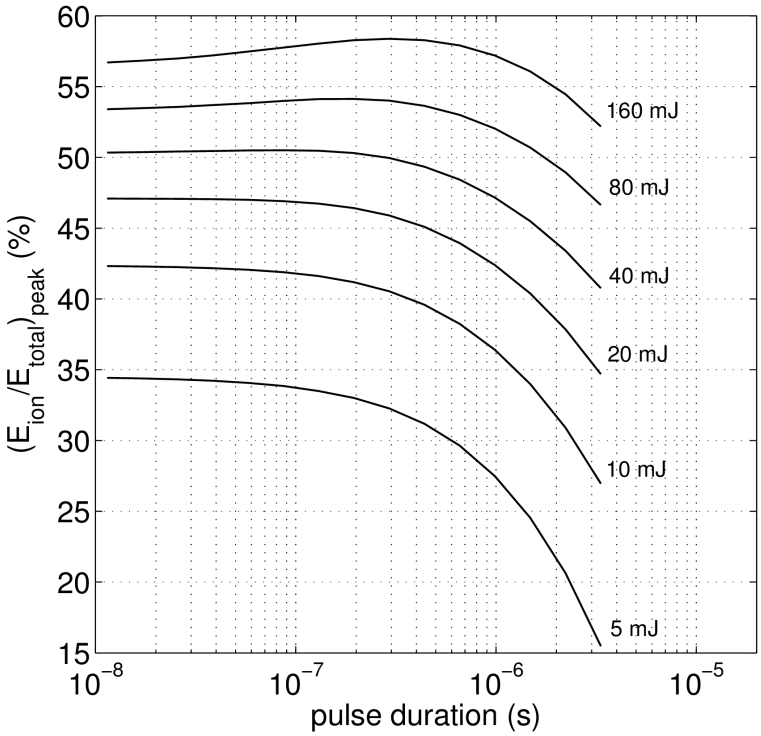

Figure 2.8: Peak IEF for varied pulse duration given total energy deposition of 5 to 160 mJ.

Figure 2.8 also makes it straightforward to see multiple energy points that share a peak in IEF. For example a point on the 40 mJ data series in Figure 2.8 shows an IEF peak of 40.8% with a pulse duration of 3.33×10^{-6} seconds while a point on the 10 mJ data series shows nearly the same IEF peak at 40.6% with a pulse duration of approximately

an order of magnitude less at 2.93×10^{-7} seconds. While both provide the same IEF, the former uses 65% less power (12 kW versus 34.1 kW) and provides a higher peak density (1.43×10^{18} m^{-3} versus 0.54×10^{18} m^{-3}) at the cost of a higher total input energy.

Figure 2.9 shows conductivity over time for all six energies tested. Similar to the results for varied pulse duration all cases start at a conductivity of 3.8 $m\Omega^{-1}$ m^{-1}. Because an increase in energy for a set pulse duration means an increase in power, the trends of Figure 2.9 are very similar to those of Figure 2.7 in which the conductivity experiences first a drop to a minimum value followed by a rebound increasing conductivity to the power-off time and then a further increase before leveling out to a final value. The main difference from Figure 2.7 however is the greatly increased final conductivity for increased total input energy. Specifically, for the high energy case of 160 mJ a minimum first occurs of 0.25 $m\Omega^{-1}$ m^{-1} at 0.05 μs. Then at power-off of 2.2 μs the high energy case reaches a conductivity of 8.9 $m\Omega^{-1}$ m^{-1}. Upon power-off, conductivity continues to increase until plateauing to a large final value of 47 $m\Omega^{-1}$ m^{-1}. Figure 2.9 also highlights that each doubling of energy is shown to yield an equivalent conductivity at consistently earlier times. The final conductivity of 1.7 $m\Omega^{-1}$ m^{-1} for the low energy case is matched by each higher energy case at approximately 3.5, 2.6, 2.0, 1.6, and 0.7 μs, for 10, 20, 40, 80, and 160 mJ, respectively.

2.3.4. Constant Power Analysis. In addition to the analyses that the preceding sub-sections provide, some further investigations into the relationship between metrics are performed with the variance in pulse duration and energy. Specifically, both duration and energy are adjusted to provide a constant *power* analysis. These studies focus on 10, 20, 50, and 100 kW of constant power and employ an initial energy of 5 mJ, initial seed

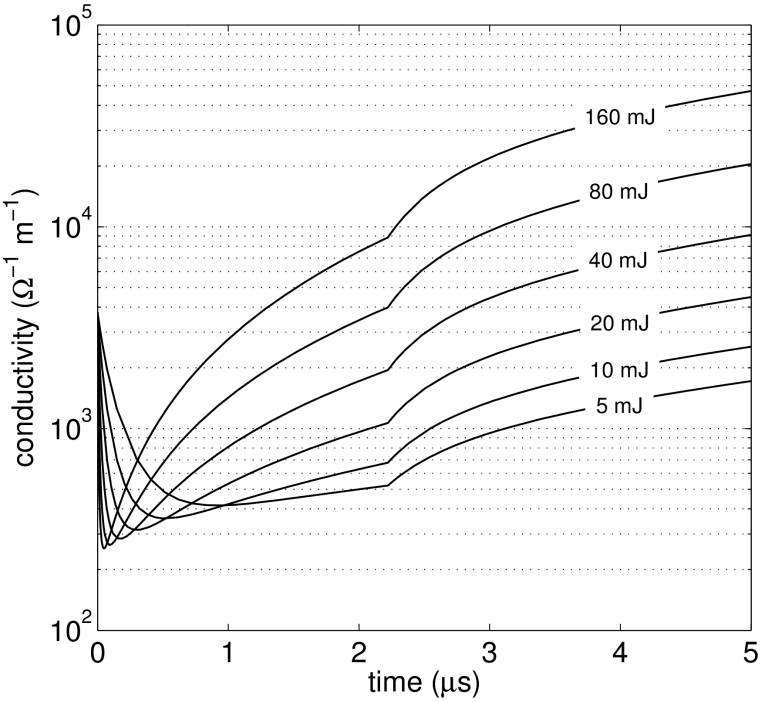

Figure 2.9: Plasma conductivity over time given total energy deposition of 5 to 160 mJ (fixed pulse duration of 2.2 μs).

density of 10^{15} m^{-3}, and maximum pulse power duration of 10 μs. An initial seed density of 10^{15} m^{-3} was chosen based on analysis presented in earlier work [51] which has shown that the largest IEF can be maintained out to approximately this initial plasma density. To clarify the iterative process, input energy is started at 5 mJ for each fixed power yielding a duration given by

$$\Delta t = \frac{E_{total}}{P_{abs}}. \tag{13}$$

Energy is then incrementally increased yielding an increased pulse duration to maintain fixed power. This is repeated until a maximum pulse duration of 10 μs is reached.

Figure 2.10 shows a comparison between times for peak IEF and peak conductivity. In the plot, going from bottom left to top right, total energy and pulse duration are increased to provide constant power and each data point represents a single

simulation's peak value times. Also shown in the plot is a 1:1 dashed trendline extending from the bottom left to the top right in the plot. Data below this line represents cases where IEF peaks before conductivity. This line shows that the time to peak conductivity consistently occurs approximately 1 to 2 μs later. The shortest times occur around 3.1 and 1.0 μs for peak conductivity and IEF, respectively. While the longest times occur around 11.5 and 9.8 μs for peak conductivity and IEF, respectively. Figure 2.10 conveys the result that over all durations, energies, and powers tested, peak conductivity consistently lags behind peak IEF.

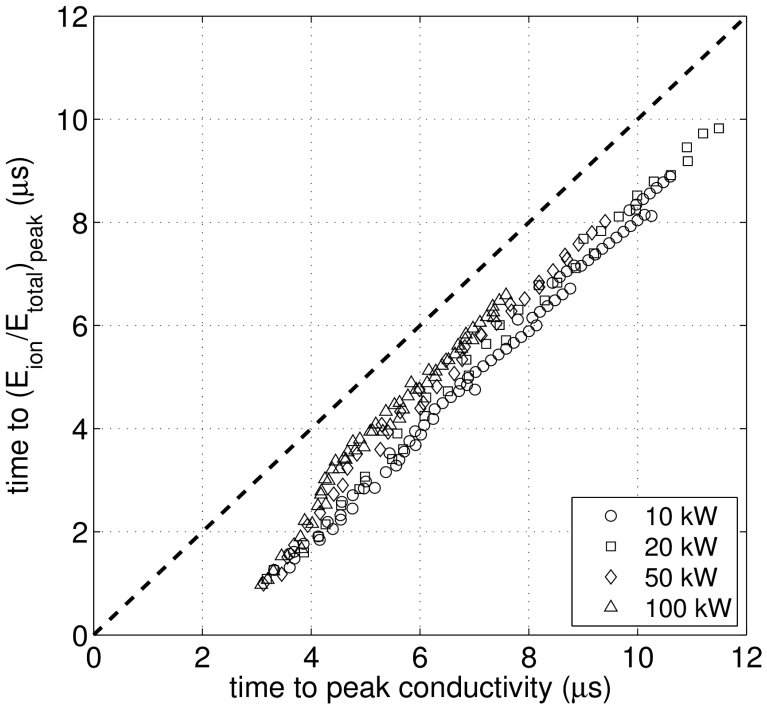

Figure 2.10: Times for peak IEF and peak conductivity. Dashed line represents equal peak time.

Figure 2.11 shows peak IEF against peak conductivity over several runs at the four power cases. To be clear, data contained in each curve represent values of peak conductivity and corresponding peak IEF for each iteration of increased energy and pulse duration. As mentioned above these never occur at the same time during the pulsed

discharge and all peak value pairs have a 1 to 2 μs lag between them with IEF occurring first, per results in Figure 2.10. Inspection of the four fixed power profiles reveals significant differences in trend as power is increased from 10 to 100 kilowatts. For the low power case of 10 kW a starting conductivity of 0.32 $m\Omega^{-1}\ m^{-1}$ yields a peak IEF of 48% and decreases rapidly before reaching a minimum of 41% at 4.5 $m\Omega^{-1}\ m^{-1}$. The next power level of 20 kW starts at a conductivity of 0.32 $m\Omega^{-1}\ m^{-1}$ yielding a peak IEF of 49%. The 20 kW power profile also decreases rapidly at low pulse durations similar to the 10 kW case, however then begins to level out and actually increases slightly to a local maximum of 47% at 6.2 $m\Omega^{-1}\ m^{-1}$ before once again decreasing, eventually reaching a minimum of 44% at 11 $m\Omega^{-1}\ m^{-1}$. The 50 kW profile also starts at a conductivity of 0.32 $m\Omega^{-1}\ m^{-1}$ yielding a peak IEF of 49%. Contrary to the 10 and 20 kW cases, the 50 kW case immediately begins to increase providing higher IEFs for increased conductivity. This trend plateaus briefly before again increasing out to a profile maximum of 53% at 12 $m\Omega^{-1}\ m^{-1}$. Energy fraction then begins to decline steadily until reaching a final minimum value of 49% at a conductivity of 24 $m\Omega^{-1}\ m^{-1}$. The high power case of 100 kW again shows an immediate increase in both peak IEF and peak conductivity, this time without the initial plateau. Profile maximum is also drawn out to higher conductivities reaching a maximum of 57% at 19 $m\Omega^{-1}\ m^{-1}$. The high power case then begins to decrease at similar rate as the 50 kW case reaching a final value of 51% at 41 $m\Omega^{-1}\ m^{-1}$. Constant power of 100 kW provides an increase in IEF of 4% over 50 kW constant power and an increase of 10% over 20 kW (using the local maximum at 6.2 $m\Omega^{-1}\ m^{-1}$). When moving from left to right in Figure 2.11 there is an increase in input energy (as well as pulse duration governed by (13)) yielding increased ion densities and hence increased conductivities.

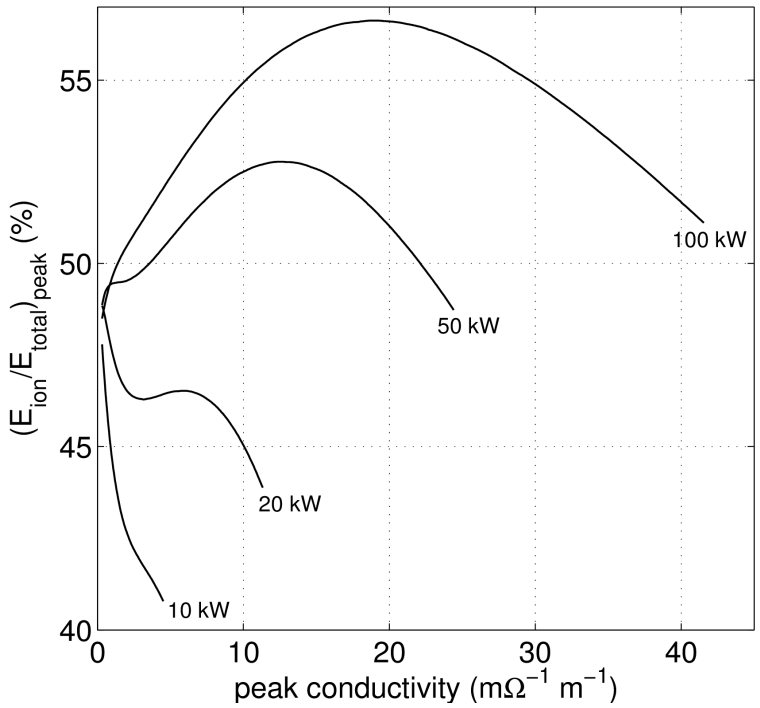

Figure 2.11: Peak conductivity and corresponding peak IEF for fixed time-average power (fixed initial seed electron and ion densities of 10^{15} m^{-3}).

2.4. SUMMARY

Reduction of pulse duration alone (keeping total absorbed energy fixed) is shown to increase peak IEF (i.e., the percentage of input energy entrained in ions) by 17% (from 16% to 33%) for reduction of duration time from 10^{-6} to 10^{-7} seconds. In pulsed inductive plasma accelerators increased plasma conductivity provides for a greater inductive coupling during the main bank discharge. The demonstrated drop in duration increases peak conductivity by 21%. Increases in total energy deposited also increases IEF from 16% at 5 mJ to 53% at 160 mJ for a 3.3 μs pulse duration. The largest IEF of 58% is seen for the 160 mJ high energy case. Across all pulse durations IEF increases for increased input energy however, this trend appears to diminish with IEF appearing to approach a ceiling near 65% as energy increases exponentially. Final conductivity shows a direct linear dependence on input energy with a slope averaging 239 Ω^{-1} m^{-1} per

millijoule. Additionally, it is observed that the same peak IEF can be achieved (about 40.6%) for power levels ranging from 12 kW to 34 kW. Fixed power analysis shows that IEF plateaus for increasing plasma conductivity and peak conductivity consistently occurs 1 to 2 μs later than peak IEF. Specifically for a high power system of 50 kW, peak IEF maximizes at 53% for conductivity around 13 $m\Omega^{-1}\ m^{-1}$. For a state-of-the-art EP system of 100 kW, maximum peak fraction only gains an additional 4% (plateauing at 57%) for a 48% higher conductivity of 19.2 $m\Omega^{-1}\ m^{-1}$. Additionally, these plateaus in IEF occur near the middle of pulse durations/energies tested rather than the end, showing a steady decrease for higher peak conductivities. These increased conductivities are a direct result of increased ion densities due to larger total input energy. Alternatively for a lower power system of 10 kW or less, peak IEF and peak conductivity show an inversely proportional relationship as highlighted in Figure 2.11.

3. PULSED THETA-PINCH WITH BIAS MAGNETIC FIELD

3.1. PROBLEM STATEMENT AND ASSUMPTIONS

Before ionization studies were undertaken efforts were made to ensure reasonable accuracy of the code and proper implementation of the particle physics. The geometry parameters used were a characteristic length of half the total length of FRCHX, or 18.2 cm and a constant radius of 6.5 cm. These parameters were chosen to capture the mid-section of a theta-pinch coil like FRCHX and provides a simulation length to diameter ratio, L/D=1.4.

Three principle assumptions were used in the simulations and analyses presented here. These are; (1) fields consist of only a uniform, axial magnetic field and an azimuthal electric field, (2) the problem is static (i.e., fields are constant) over short time intervals of approximately 10 nanoseconds, and (3) fields follow the planar simplification: $\mathbf{B} = B_x(t)\,\hat{x}$ and $\mathbf{E} = E_z(y,t)\,\hat{z}$. Assumption (1) simply implies that end effects such as magnetic mirror, diverging electric fields, etc., are ignored. Assumption (2) is justified in a window of 10 nanoseconds for this study by reported results of FRCHX (Figure 1.2). In these results, during the first ¼ cycle of the pre-ionization ring, the magnetic field is seen to decrease sinusoidally from an initial value of 500 mT to approximately zero in 1 μs. This corresponds well with a reported pre-ionization circuit frequency of 230 kHz ($t_{1/4} \approx 1.09$ μs). From here it is assumed that 10 ns << $t_{1/4}$ and subsequently $B(t) \approx B(t+10\text{ ns})$. Additionally, the internal time-step used by the XOOPIC solver was assigned to be 1×10^{-12} s. This time-step falls well under the period of the largest gyro-frequencies seen of approximately 70.0×10^{-12} s. The solver package XOOPIC will be discussed in section 3.3 of this document. The assumption (3) of planar

fields (**B**=B_x, **E**=E_z) stems from a focus here on an *r*-*z* plane which is then converted to an analogous Cartesian geometry as shown in Figure 3.1. While XOOPIC is able to natively run simulations in cylindrical coordinates the verifications described in this section as well as all following studies were performed using a Cartesian coordinate approximation limited by the assumption that azimuthal (out of the *r*-*z* plane) travel by electrons is small at all times of interest (t = 0 to $t_{1/4}$). This was done to avoid erroneous results from inputting azimuthal electric fields (i.e., $\nabla \times E \neq 0$) into a static solver. By extension, this assumption also implies the common use of azimuthal symmetry and ignores bulk motion azimuthally. Motions that could be due to (for instance) diamagnetic drifts as density becomes non-uniform.

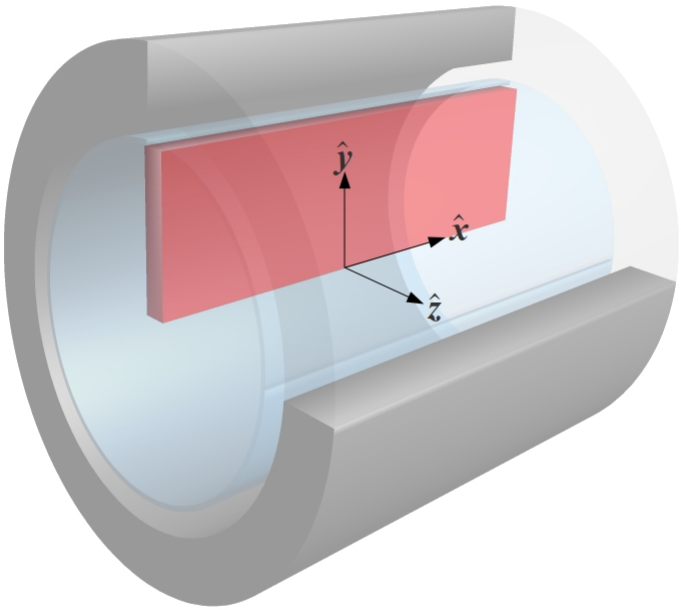

Figure 3.1: Analogous Cartesian geometry simulated (red) using planar approximation, overlay with Figure 1.1.

A sinusoidal magnetic field profile and simple ideal solenoid analysis is used, along with Faraday's law, to provide the connection between induced electric fields and

time varying magnetic fields. The resulting fields are modeled after reported results from FRCHX. Nomenclature for Faraday's Law in a theta-pinch device follows with common ideal solenoid analyses. For uniform, orthogonal fields equation (14) is simplified to (14) for approximation of the electric field magnitude.

$$E(r,t)=\left(\frac{-dB}{dt}\right)\frac{r}{2}\ \text{(V/m)} \tag{14}$$

Magnetic field is modeled by an inverted sine function with positive offset matching initial bias of 500 mT. Device frequency, *f*, is approximated to be 250 kHz (actual frequency reported to be approximately 230 kHz in FRCHX test article [41]) yielding the appropriate ¼ cycle time of 1 μs.

$$B(t)=-0.5\sin(2\pi f t)+0.5\ \text{(T)} \tag{15}$$

Plots of approximated field profiles can be seen overlaid with FRCHX results in Figure 3.2 for an ambiguous radial value. From here cylindrical coordinates are approximated to Cartesian coordinates by the nomenclature seen in Figure 3.1. For clarity this transition is also stated in equation (16).

$$\begin{Bmatrix} B(t)\hat{z}_{cyl}\rightarrow B(t)\hat{x}_{cart} \\ E(r,t)\hat{\theta}_{cyl}\rightarrow E(y,t)\hat{z}_{cart} \end{Bmatrix} \tag{16}$$

3.2. SINGLE PARTICLE MODELING

Preliminary modeling of the single particle kinetics in time-varying electric and magnetic fields was performed prior to simulation and analysis of the problem statement with XOOPIC. This initial approach serves two purposes. First it provides insights into the final state magnitudes that should be anticipated for the bounded geometry, multi-

species simulations. Second, it provides an additional measure of verification for the XOOPIC code. In this study, the particle is not bounded and is free to move as fields dictate.

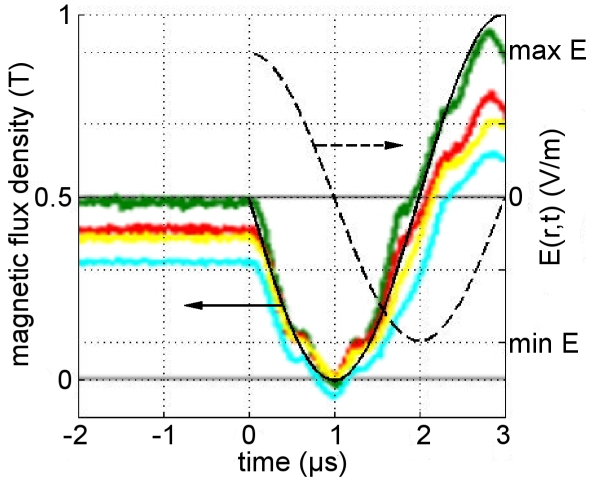

Figure 3.2: Reconstructed field profiles with original reported FRCHX results.

Single particle motion is modeled and simplifies to differential equations (17) and (18) for two dimensional oscillatory motion in uniform orthogonal fields. The $\hat{y}$ and $\hat{z}$ directions here correspond to those depicted in Figure 3.1 and are re-iterated as being perpendicular to an axial magnetic field.

$$\frac{d\vec{v}_y}{dt} = \frac{e}{m_e}\left(0 + v_z \cdot B_x\right)\hat{y} \tag{17}$$

$$\frac{d\vec{v}_z}{dt} = \frac{e}{m_e}\left(E_z - v_y \cdot B_x\right)\hat{z} \tag{18}$$

Magnetic field starts at 500 mT and decreases sinusoidally to zero at 1 μs as seen for the FRCHX data. Because electron motion is unbounded for this single particle study, electric field is not varied with position as depicted in equation (16) and is instead fixed for a value of y=3.25 cm corresponding to a radial value in FRCHX of $R/2$. Thus $E(y,t)$

$\rightarrow E(t)$ at $y = 3.25$ cm and starts at a value of 12.76 kV/m varying sinusoidally with time only, crossing zero at 1 μs.

3.3. PARTICLE-IN-CELL (PIC) METHODS

3.3.1. Code Verification. The freely available UniX based Object-Oriented Particle-In-Cell code XOOPIC [57,58] developed originally at U.C. Berkley, is utilized to model ionization at early times in a deuterium gas for pseudo theta-pinch geometry. This code is a 2-D, relativistic, Monte Carlo collisional code that can be modeled electrostatically or, if curling electric fields lie only on a 2-D solution plane, can solve electrodynamic problems as well. Verification of particle kinetics in Cartesian coordinates is performed first to verify unmodified PIC code with theory. These verifications include analysis of; (1) electron-cyclotron frequency, (2) Larmor radius, and (3) $\boldsymbol{E}\times\boldsymbol{B}$ drift velocity. Collisions were effectively turned off and no electric fields were prescribed, assigning only an initial azimuthal velocity. Tabulation of the particle position by XOOPIC at each time step, in this case 1.0×10^{-12} seconds (0.001 ns), allows for re-construction of the electron trajectory and subsequent extrapolation of both gyro-frequency and gyro-radius. Additional analysis of the guiding center motion provides an estimation of drift velocity.

Electron-cyclotron frequency, $f_{c\ theory} = \frac{eB}{2\pi m_e}$ (Hz), is defined for magnetic field magnitude, B, and electron mass, m_e ($\approx 9.11\times10^{-31}$ kg). For a magnetic field of 100 mT the electron-cyclotron frequency found in PIC simulation yields a percent difference of less than 1% against theory. Larmor radius for electrons is, $r_{L\ theory} = \frac{m_e v_\perp}{eB}$ (m), where $v_\perp$ is the total velocity perpendicular to the magnetic field. Initial particle velocity components were user specified as 8×10^{6} m/s in the axial direction alone. Using this velocity and 0.1

T magnetic field $r_{L,theory}$ is obtained and reported in Table 3.1 along with an r_L value from XOOPIC output. Again percent difference between theory and simulation is less than 1%. To verify proper $\boldsymbol{E}\times\boldsymbol{B}$ guiding center (GC) drift motion a uniform electric field orientated in the $\hat{z}$-direction (perpendicular to the analogous **red** Cartesian plane in Figure 3.1) is applied to the above case providing a GC drift in the $\hat{y}$-direction. Here initial velocity is removed to allow for acceleration by the applied electric field only. For $\boldsymbol{E}\times\boldsymbol{B}$, GC drift velocity magnitude simplifies to $v_{\boldsymbol{E}\times\boldsymbol{B}\ theory}=\frac{E}{B}$ for orthogonal field vectors. For a 25.5 kV/m applied electric field and 0.1 Tesla magnetic field the theoretical GC drift velocity is shown along with the estimated velocity from PIC simulation. As with gyro-frequency and Larmor radius, percent difference between theory and simulation vary by less than 1% as shown in Table 3.1.

Table 3.1: Verification of electron-cyclotron frequency, gyro-radius, and $\boldsymbol{E}\times\boldsymbol{B}$ guiding center drift velocity

100 mT bias field	
$f_{c,\ theory}$	2.79 GHz
$f_{c,\ PIC}$	2.80 GHz
percent difference	0.36%
100 mT bias field, initial velocity of 8×10^6 m/s	
$r_{L,\ theory}$	456 μm
$r_{L,\ PIC}$	460 μm
percent difference	0.88%
100 mT bias field, 25.5 kV/m electric field	
$v_{\boldsymbol{E}\times\boldsymbol{B},\ theory}$	255.25 km/s
$v_{\boldsymbol{E}\times\boldsymbol{B},\ PIC}$	255.61 km/s
percent difference	0.14%

3.3.2. Iterative PIC Scheme. XOOPIC's electrostatic solver is used for these studies because electric field curls azimuthally (i.e., in/out of the *r-z* plane). The iterative

approach used for running XOOPIC with static fields was adopted out of the necessity to be able to completely control time-varying electric fields directed normal to the plane of simulation. The iterative scheme in brief involves; (1) running XOOPIC for a short duration (i.e., 0.005 to 0.01 μs) with zero initial electron velocity, (2) exiting XOOPIC and writing all electron/ion positions/velocities to file upon exit, (3) post-processing an average velocity for electrons, and (4) returning to step 1 with the calculated average electron velocity applied as the new initial electron velocity for all electrons in the system. In these studies ions created (which were very few, if any) are discarded, beginning each new iteration with the initial electron population of 10^{12} m^{-3} and zero ions. Any electrons lost to boundaries are not involved in post-processing and are reset (in terms of position) at the beginning of the next iteration.

3.4. RESULTS AND ANALYSIS

3.4.1. Single Electron Energy Results. Figure 3.3 shows kinetic electron energy data for the applied fields shown in Figure 3.2. For an assumed initially "cold" electron, kinetic energy starts at zero and varies minimally until approximately 0.9 μs. For this reason Figure 3.3 focuses on a time frame of 0.85 to 1.1 μs only. By 0.9 μs the applied magnetic field, as seen earlier in Figure 3.2, has been reduced by nearly 99% from 500 to 6.2 mT, compared with 84% for the electric field (12.76 to 2.0). Just 37 nanoseconds after the magnetic field zero-crossing (i.e., $t_{1/4}$+0.037 μs), oscillatory electron energy crosses the gaseous D_2 ionization threshold, $I_{g,D2}$, of 15.47 eV. Following this, at approximately 1.05 μs, energy peaks at 32.2 V (not shown) corresponding to a velocity magnitude of 3.35×10^6 m/s. This time at which energy peaks corresponds to a field magnitude of 1.5 mT which, when combined with velocity magnitude, yields a Larmor radius of 1.2 cm.

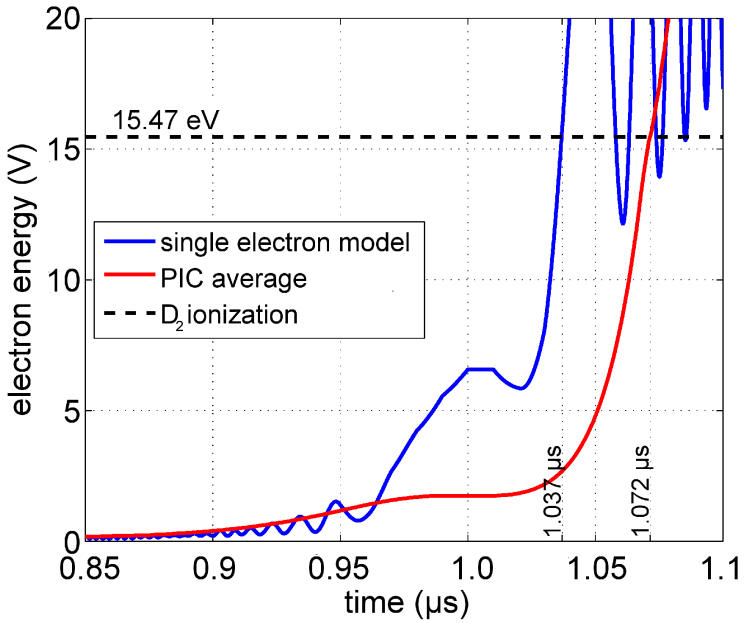

Figure 3.3: Kinetic energy for both single electron energy study and iterative PIC study. Initially cold (i.e., velocity = 0 m/s) electrons.

This simple analysis of the single electron kinetics for orthogonal time-varying fields shows that, from rest and for the field profiles approximated from FRCHX data, the electron only achieves deuterium level ionization energies just after magnetic field goes to zero. This agrees qualitatively with reported ionization results of FRCHX. However it is worth restating that in this simple analysis a single radial location was used thus ignoring the transition to higher electric field magnitudes as electrons drift radially outward by $\boldsymbol{E}\times\boldsymbol{B}$ GC drifts. A common physical result of real theta-pinch devices. Also no boundary conditions were set keeping electron energy from being lost to the walls nor is a background gas present to allow energy loss via collisions as electrons approach the deuterium excitation energy (≈14.9 eV).

3.4.2. Iterative PIC Results. Figure 3.3 also shows results from the iterative PIC approach outlined above against the earlier single electron results. In these tests both elastic and ionization collisions are modeled and remove some energy from the super-

thermal, or near-beam energy distribution around and after quarter-cycle time, $t_{1/4}$. Loss of electron energy to excitation and ionization collisions, is suspected by the authors to be the cause of the difference in time the ionization threshold is reached between the single particle and PIC study ($t_{1/4}$+0.037 μs vs. $t_{1/4}$+0.072 μs, respectively). It can be seen from Figure 3.3 that while average energy lags that of the single particle case, trends of the PIC study still correspond with the delayed ionization reported by FRCHX. It should be noted that a deuterium collisional cross-section table was not natively available in XOOPIC and thus the table for gaseous diatomic hydrogen ($I_{g,\mathrm{H2}}$ = 13.6 eV) was used as a substitute in these particle-in-cell studies.

3.4.3. Parametric Study In B_{bias}-B_{PI} Space. To analyze additional experiments a parametric study using the above single particle approach has been conducted by revisiting equation (15) and generalizing for a time-varying net magnetic field,

$$B_{net}(t) = -B_{PI}\sin(2\pi f t) + B_{bias}\ (\mathrm{T}). \tag{19}$$

Here B_{PI} denotes amplitude of the pre-ionization, however this component can represent a main discharge as well if PI is not present. To fill out a 3-d performance space, B_{bias} and B_{PI} magnitudes are varied individually and peak electron energy is found and plotted for all combinations therein. In all combinations, electric field has been evaluated in the same manner as above, which is that the electric field at half radius (3.25 cm) is used. In the interest of computation time, three ranges for B_{bias} and B_{PI} are assigned individually and data are then spliced together post-process. This is evidenced by the three squares of color data in Figure 3.4 overlapping at the corners corresponding to the three ranges tested. The area of 'white-space' above-left and below-right in Figure 3.4 was not simulated, but trends in these areas can be extrapolated from the investigated regions.

Field magnitude ranges tested were: B_{bias}, B_{PI} = 0-350, 300-700, and 650-1050 mT. Ranges were picked to overlap by 50 mT to verify smooth transition of values from one data-set to the next.

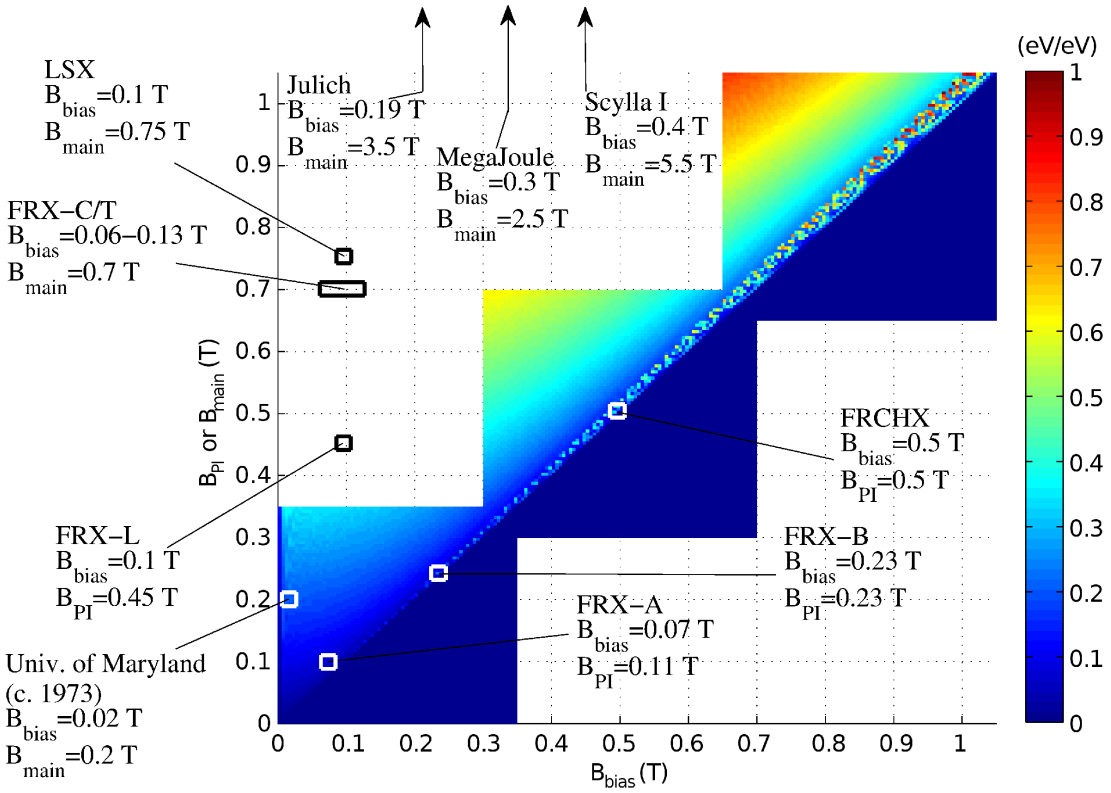

Figure 3.4: Peak electron energy (normalized to maximum of 1600 eV) for varying bias and pre-ionization magnetic fields. Overlaid with performance data points from various theta-pinch test articles.

Figure 3.4 shows the results of this additional analysis by plotting the maximum electron temperature (normalized to 1600 eV) seen in each combination of B_{bias} and B_{PI}. Values in the figure are the first electron peak in the discharge cycle (i.e., only the first ½ cycle has been modeled). With some explanation it can be seen from Figure 3.4 that three regions of electron energy activity arise. First is a region of low peak electron energy for the case of $B_{bias} \geq B_{PI}$ seen starting in the lower right of each range of field values (shown in darker blue in the lower-right of each data set). In this region net magnetic field is either not nullified and a zero-crossing never occurs or is just made to

reach zero as electric field does so at the same time (i.e., $B_{net} = 0$ as $dB_{net}/dt = 0$). Subsequently electron energy remains low (or just approaching ionization levels). This region is where FRX-B and FRCHX are operated. Transitioning then to a second region in Figure 3.4, where B_{bias} consistently falls just below B_{PI} ($B_{bias} \approx 97\%$ of B_{PI}) yields a semi-random distribution of high energy values cutting diagonally through the figure from bottom left to upper right. It is noted here that verification that this region was not the result of numerical error or non-convergence was addressed. Electron energy profiles over time for these B_{bias}, B_{PI} values appeared smooth and only the result of constructive (or destructive) timing between gyromotion and zero-crossing(s). Theta-pinch test articles operated in this region capitalize on the consequence of the sinusoidal nature of the field profiles (see Figure 3.2), wherein magnetic field is reduced significantly earlier as time approaches $t_{1/4}$ while electric field remains high for these times (for instance $E(t_{1/8}) = 71\%$ of E_{max} while $B(t_{1/8}) = 29\%$ of B_{max}). This provides a short time frame where electrons are able to accelerate under a large electric field while relatively unrestricted by magnetic field. The stark contrast between these first two regions reveals that a brief zero-crossing gives electrons a small amount of extra acceleration time before electric field passes through zero. Unfortunately, timing of both net field zero-crossing and gyromotion become critical in this second region and peak electron energies prove to be quite erratic with respect to B_{bias}-B_{PI} space. It should be noted however, that for an actual multi-particle environment this "peppering" of high energy cases in the second region (where $B_{bias} \approx B_{PI}$) would be smoothed significantly by collisional processes and peak energies in this region will most likely be dictated by (and inversely proportional to) backfill gas pressure. Finally a third region follows for further reduced B_{bias} ($B_{bias} < 0.97B_{PI}$, or equivalently an increased B_{PI}), and peak energy trends as a smooth gradient of

increasing peak electron energy for increased B_{PI}/B_{bias}. Here net magnetic field passes through zero at earlier times while the electric field profile remains unchanged, for instance when considering a line of decreasing B_{bias} for constant B_{PI} (because electric field is only a function of B_{PI} magnitude and discharge frequency). This appears to be the ideal region in which to operate a theta-pinch based on it's desirably well-behaved and predictable peak energy trend. However, as electric field is increased (i.e., larger dB/dt, leading to greater particle acceleration) for earlier zero-crossing net magnetic field, charged particle losses to the walls of the device would become the predominant concern.

Figure 3.4 also shows design point call-outs corresponding to field magnitudes reported from previous theta-pinch experiments. It is noted here that a PI discharge is not present in all theta-pinch test articles (such as early theta-pinch experiments of the 1960's) and in these cases where PI is not present B_{PI} magnitude represents instead the main inductive discharge magnitude. Thus it is re-iterated that "post-bias" simply refers to whichever discharge immediately follows bias field application. It is also noted that this analysis assumes the post-bias inductive discharge, whether it be PI or main, is timed to occur at the peak of the bias field. If this is not the case then B_{bias} here would represent the magnitude of the bias field at the time of discharge for the post-bias field. Additionally, while the results of Figure 3.4 are for a constant post-bias field frequency of 250 kHz, the trends seen here have been verified to hold for both 125 kHz and 500 kHz with the only difference being a shift up (for higher frequencies, larger dB/dt) or down (for lower frequencies, smaller dB/dt) in peak energies uniformly. It is concluded then that the characteristic regions described for Figure 3.4 are repeatable over the entire frequency range of typical theta-pinch post-bias coil discharges.

Analysis of Figures 3.2 and 3.4 is used to study how the electric field magnitude at the time of the net magnetic field zero-crossing changes as a function of B_{bias} and B_{PI}. Figure 3.5 shows this relationship for constant pre-ionization magnetic field (B_{PI} = 0.05, 0.3, 0.55, 0.8, and 1.05 T shown) and it can be seen that the highest values for electric field occur as bias field offset, B_{bias}, approaches zero (left side of the figure). This becomes obvious when referred back to Figure 3.2 and one pictures net magnetic field as initial bias field offset is reduced. Net magnetic field crosses zero at earlier times and electric field corresponding to these earlier times is higher (because dB/dt is larger) thus yielding the results of Figures 3.4 (in the 3rd region of Figure 3.4 described above where B_{bias} = 40% to 60% of B_{PI}) and 3.5. Across all cases electric field at net magnetic field zero-crossing remains above approximately 90% of the maximum for B_{PI} to B_{bias} ratios of 2 to 1 or higher. The reader is reminded that electric field as defined in this work is affected by B_{PI} and frequency only. Conversely as B_{bias} approaches a given B_{PI} electric field is reduced to zero. Again this is explained by reference to Figure 3.2. As B_{bias} approaches the same value as B_{PI} (e.g., as one approaches the conditions of FRCHX), electric field at B_{net} zero-crossing converges on the value at $t_{1/4}$. This is of course where dB/dt = 0 and subsequently E(y,t)=0. Increased B_{bias} past B_{PI} means that B_{net} zero-crossing never occurs and thus electrons never see the (albeit brief) period of unrestricted acceleration and electron energies remain very low. This corresponds to the first region described above for Figure 3.4.

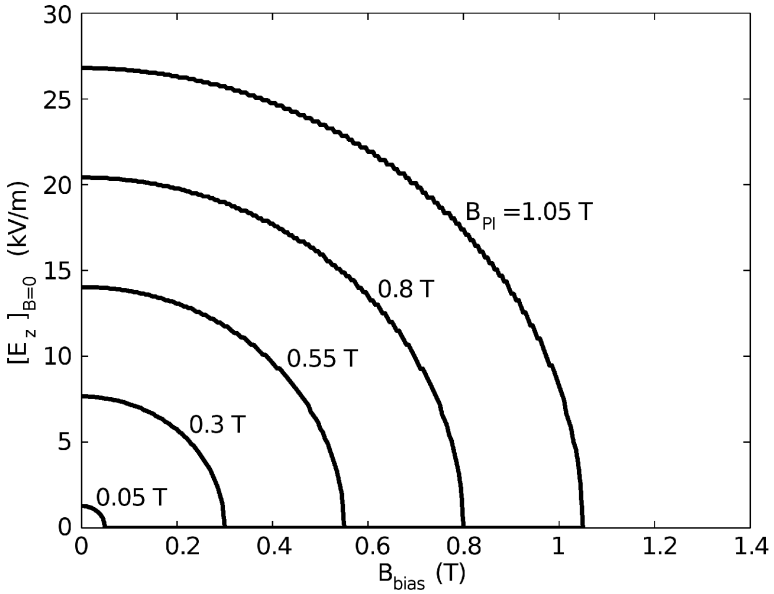

Figure 3.5: Electric field magnitude at the time of net magnetic field zero-crossing for select lines of constant pre-ionization magnetic field.

4. CONCLUSIONS

4.1. CONCLUSIONS OF THE RF PRE-IONIZATION STUDY

Two primary conclusions are observed from the RF pre-ionization studies; 1) that regardless of power level a time delay between highest fraction of input energy in ions and highest level of conductivity is unavoidable, and 2) that better coupling plasmas (higher conductivity) at the end of RF pre-ionization can be achieved however, at the cost of a less efficient use of power (energy). The consequence of point one becomes apparent when considering the operation of a pulsed ICP acceleration device such as an EP thruster in which typically timing of the next stage is driven by maximization of inductive coupling between the plasma and this next stage. This ensures the greatest amount of energy being transferred from the circuit hardware to the plasma. Based on the first conclusion, coupled with this timing criteria, the fraction of ion energy to input energy (the IEF) upon discharge of the next stage will consistently fall short of the highest fraction seen by the system. The consequence of point two becomes apparent when considering the design process of an EP thruster in which the desire to keep the percentage of losses (i.e., excited species creation, diffusion to walls) to a minimum can become paramount and thus Figure 2.11 imposes a ceiling for scalability of an RF pre-PI stage. For example, if a 50 kW pulsed RF PI source with a peak IEF of no less than 50% is desired then the source will not yield a pre-ionization plasma with more than approximately 23 $m\Omega^{-1}$ m^{-1} conductivity. Alternatively, for lower power (<10 kW), peak RF source-energy percentage entrained in ions will consistently reduce as higher levels of peak conductivity are achieved.

4.2. CONCLUSIONS OF THE BIAS THETA-PINCH IONIZATION STUDY

Reported results from several theta-pinch experiments arrive at the same conclusion that ionization can be dictated (i.e., inhibited) by improper choice of bias magnetic field magnitude and the post-bias stage that follows (pre-ionization or main discharge, depending on the device). This fact is further substantiated by single particle and particle-in-cell studies presented here. These models were first verified against each other yielding 37 and 72 ns delays (past quarter-cycle discharge time) in reaching gaseous deuterium ionization levels for single particle and particle-in-cell studies, respectively, each using FRCHX design characteristics. Subsequently, further inspection against FRCHX has shown good qualitative agreement from both models with reported results from Grabowski *et al* (2011).

Additional simulation studies were performed to better describe the relationship between electron energy and (bias and post-bias) magnetic field magnitudes. Specifically demonstrated in this work is that electron energy remains minimal until the pre-ionization or main field magnitude is at least approximately 3% higher than bias field. In general, having this larger post-bias discharge magnitude over that of the bias is shown to allow a critical net magnetic field zero-crossing which proves imperative in triggering high level electron energies. In addition, it is demonstrated that a near-matched set of bias and post-bias field magnitudes does not yield well-behaved and predictable electron energies making designed performance difficult to impossible. Also it is shown graphically that electric field present during the zero-crossing of the net magnetic field is increased for decreased bias field magnitude. Ultimately, results presented here show that a desired ratio of post-bias to bias magnetic field magnitudes is on the order of 2 to 1 or higher.

APPENDIX A

BASE CODE USED FOR COMPARISON AGAINST ASHIDA ET AL. [47] REPORTED RESULTS AND FURTHER RF PRE-IONIZATION MODELING

Octave file *Ashida_mod.m* which calls the *d_dtwPower.m* and *d_dtw_oPower.m* files as functions in the ODE solver;

```
%% filename:  Ashida_mod.m
% author:     Warner C. Meeks
% contact:    wcm994@mst.edu
% advisor:    Joshua L. Rovey (roveyj@mst.edu)
% affiliation:Missouri University of Science and Technology, Aerospace
Plasma Lab, Aerospace Engineering Dept.
% purpose:    MPX related, global model of argon for time evolution of
plasma parameters given a known power input
% references: 1) Ashida, Lee, and Lieberman, "Spatially averaged
(global) model of time modulated high density argon plasmas," J.of
Vac.SciTech, Vol.13, pg.2498 (1995)
%             2) Rapp, and Englander-Golden, "Total Cross Sections for
Ionization and Attachment in Gases by Electron Impact," J.of Chem Phys,
Vol.43, pg.1464 (1965)
%             3) Lieberman, and Lichtenberg, "Principles of Plasma
Discharges and Materials Processing," 2nd ed, (2005)
%             4) Kirtley, "Study of the Synchronous Operation of an
Annular Field Reversed Configuration Plasma Device," Ph.D Thesis
presented to the Dept. of Aerospace Engineering, University of
Michigan, Ann Arbor, MI (2008)
% dependencies: d_dtwPower.m, d_dtw_oPower.m
% NOTES:   modified to run in GNU Octave v3.2.3
%        http://www.gnu.org/software/octave/

close all
clear all
clc

%% CONSTANTS:
  global P_abs rate_set

%% TIME MANAGEMENT:
  t1 = clock; % for program duration checking only, not used in
calculations
  time_step = 1D-7;

%% INITIAL CONDITIONS:
  % GAS IC's:
% 10 microsecond case
%{%
  time_total = 10.0D-06;  %[sec]
  time_off = time_total*0.25;
  n_g0 = 8.0D19; % [m^-3]  (P=nkT, P=5mTorr, T=273.15, yields n~1x10^20
m-3)
  nex0 = 1.0D17;
  niz0 = 2.5D17;
  n_e0 = 2.5D17; % [m^-3]  (maximum electron densities reported in
Kirtley's work of 10^18/m^3)
  Te_0 = 1.0;
    P_abs = 2000;
    rate_set = 1;  % correction factor
%}
% 100 microsecond case
```

```
%{
   time_total = 100.0D-06; %[sec]
   time_off = time_total*0.25;
   n_g0 = 8.0D19; % [m^-3]  (P=nkT, P=5mTorr, T=273.15, yields n~1x10^20
m-3)
   nex0 = 0;
   niz0 = 3.0D17;
   n_e0 = 3.0D17; % [m^-3]  (maximum electron densities reported in
Kirtley's work of 10^18/m^3)
   Te_0 = 0.5;
     P_abs = 2000;
     rate_set = 5;
%}
% 1000 microsecond case
%{
   time_total = 1000.0D-06;   %[sec]
   time_off = time_total*0.25;
   n_g0 = 8.0D19; % [m^-3]  (P=nkT, P=5mTorr, T=273.15, yields n~1x10^20
m-3)
   nex0 = 0;
   niz0 = 1.0D17;
   n_e0 = 1.0D17; % [m^-3]  (maximum electron densities reported in
Kirtley's work of 10^18/m^3)
   Te_0 = 0.5;
     P_abs = 2000;
     rate_set = 10;
%}

%% SOLVER LOOP 1:  Power ON
   Tspace1=(0:time_step:time_off);
   Y1 = lsode(@d_dtwPower,[nex0 n_e0 niz0 n_g0 Te_0],Tspace1);
%,'',P_abs,rate_set);

% In case of power ON only;
%  nex = Y1(:,1);
%  n_e = Y1(:,2);
%  niz = Y1(:,3);
%  n_g = Y1(:,4);
%  Te = Y1(:,5);

%% SOLVER LOOP 2:  Power OFF
%{%
   Tspace2=(time_off:time_step:time_total);
   Y2 = lsode(@d_dtw_oPower,[Y1(end,1) Y1(end,2) Y1(end,3) Y1(end,4)
Y1(end,5)],Tspace2);#,'',rate_set);

   nex = [Y1(:,1);Y2(:,1)];
   n_e = [Y1(:,2);Y2(:,2)];
   niz = [Y1(:,3);Y2(:,3)];
   n_g = [Y1(:,4);Y2(:,4)];
   Te = [Y1(:,5);Y2(:,5)];
%}


%% TIME MANAGEMENT (cont.)
   t2 = clock; % for runtime checking only, not used in calculations
```

```
  run_time = t2-t1;
  %disp('[hr:min:sec]');
  %disp(run_time(4:end));
  time_space = [Tspace1';Tspace2'];
% time_space = T1;
  t_s_micro = time_space./(1D-6);
```

Octave file *d_dtwPower.m* used for solving the system of differential equations where power addition is present;

```
%% filename: d_dtwPower.m
%  author: Warner C. Meeks
%  contact: wcm994@mst.edu
%  advisor: Joshua L. Rovey, (roveyj@mst.edu)
%  affiliation: Missouri University of Science and Technology, Aerospace
Plasma Lab, Aerospace Engineering Dept.
%  purpose: function called by differential equations solver , power
addition included
%  dependencies: none
%  NOTES: none

%function dydt = d_dtwPower(t,y,P_abs,rate_set) % for MATLAB
function dydt = d_dtwPower(y,t) % for OCTAVE
  global P_abs rate_set
  disp(t);  % provide output of current step
  fflush(stdout);  % prints 'disp' and 'printf' calls to screen
immediately while in loop rather than wait until loop exit
  dydt = zeros(5,1);
% CONSTANTS:
  HCS = 0.88D-20;  % [m^2]
  k = 1.3807D-23;  % [J/K] Boltzmann's const
  qe = 1.6D-19;  % fundamental charge [coulombs]
  me = 0.91D-30; % electron mass [kg]
  mu0 = pi*4.0D-07;  % Permeability of free space [V-s/A-m]
  M_gas_mol = 39.95;      % mass of gas used [g/mol]
  mgas = M_gas_mol/(1000*6.022D23);  % mass per particle [kg]
  radAr = 71D-12;  % [m] atomic radius of argon neutral
  L = 0.075;     % [m] length of cylindrical device
  R = 0.1525; % [m] radius of cylindrical device
  vol = pi*R^2*L;  % [m^2]volume of plasma assuming thin sheath
  AR = 2*pi*R^2; % [m^2]surface area of top+bottom of cylinder
  AL = 2*pi*R*L; % [m^2]surface area of side walls of cylinder
  LMDA = 1/sqrt((pi/L)^2+(2.405/R)^2);  % effective diffusion length
  E_ex = 12.14;
  E_iz = 15.76;  % from Lieberman pg.81


% DECLARATIONS:
  crs_sec = dlmread('Ar_CS_Rapp.csv',',');
  crs_sec(:,2) = crs_sec(:,2).*HCS;
  sz1 = size(crs_sec);
  area1 = 0.0;
  areaN = 0.0;
  T = 600;  % [K] neutral background temperature


% POWER INPUT:
  % fixed power input
%  P_abs = 2000;

  % fixed power square wave
  %{
```

```
  period = 10.0D-06;
  duty_ratio = 0.25;
  cycle = fix(t/period);
  uptime = t-cycle*period;
    if uptime < period*duty_ratio
      P_abs = 2000
    else
      P_abs = 0
    end
  %}

  % oscillating power via RLC circuit
  %{
  frac_trans = 1.0;  % [%] what fraction of the circuit energy actually
makes it into the plasma (via the electrons energy)
  Res = 100.0D-03; %[ohms]
  Cap = 1.0D-06; %[farads]
  Ind = 500.0D-09;   %[henrys]
  xsi = Res*sqrt(Cap/Ind)/2;
  res_freq = sqrt(1/(Ind*Cap));
  damped_freq = res_freq*sqrt(1-xsi^2);
  alpha = Res/(2*Ind);
  iknown = 800;  % [amps] maximum current(I) value @ first peak (1/4 of
period)
  t_iknown = 2*pi/(damped_freq*4);  % [sec] first peak (1/4 of period)
  const = iknown/(exp(-alpha*t_iknown)*sin(damped_freq*t_iknown)); %
determination of sine term constant
  Pwr = (const*exp(-alpha*t)*sin(damped_freq*t))^2*Res;
  P_abs = Pwr*frac_trans;
  %}


% RATE CONSTANTS:
  K0 = 2.336D-14*y(5)^1.609*exp(0.0618*(log(y(5)))^2-
0.1171*(log(y(5)))^3);  % e+Ar elastic scattering (Lieberman pg.81)
  E_elas = (3*me/mgas)*y(5);   % mean elastic energy transfer
(Lieberman pg.81)

  K1 = 2.48D-14*y(5)^0.33*exp(-12.78/y(5));  % Ar+e --> Ar*+e
  K2 = 6.88D-16*y(5)^0.33;            % Ar*+e --> Ar+e
  K3 = 2.3D-14*y(5)^0.68*exp(-15.76/y(5)); % Ar+e --> Ar'+2e  '=ionized
%  K4 = (6.8D-15*y(5)^0.67*exp(-4.20/y(5))+1.8D-13*y(5)^0.61*exp(-
2.61/y(5)))/2; % Ar*+e --> Ar'+2e (non-weighted average from Ashida
model)
  K4 = 9.34D-14*y(5)^0.64*exp(-3.405/y(5));

  A = rate_set*3.0D07*2*(1/R+1/L)/(y(4)*2.9D-16); %[1/s] Ar* --> Ar+hv
  r=resonance

  Vs = (y(5)/2)*log(mgas/(2*pi*me));  % [V]  estimated voltage drop in
sheath
  uB = sqrt(qe*y(5)/mgas);     % [m/s]Bohm velocity
  utherm = sqrt(8*k*T/(pi*mgas));

  F_E = sqrt(4*crs_sec(:,1)./(pi*y(5)^3)).*exp(-crs_sec(:,1)./y(5));
  integrand = crs_sec(:,2).*F_E;
```

```
  % descrete integration under CS data curve (sum of trapazoidal areas)
  for c0 = 1:(sz1(1)-1)
    areaN = (crs_sec(c0+1,1)-
crs_sec(c0,1))*(integrand(c0+1)+integrand(c0))/2;
    area1 = area1 + areaN;
  end
  sgma = area1;
%  sgma = 2.9D-16;
  lmda = 1/(y(4)*sgma); % [m]  estimated ion-neutral collision mean
free path
  hL = 0.86/sqrt(3.0+L/(2*lmda));% [m^-3/m^-3] ratio of axial sheath
edge plasma density to bulk electron density, from Godyak and Maximov
plane parallel discharge
  hR = 0.80/sqrt(4.0+R/lmda);  % [m^-3/m^-3] ratio of radial sheath
edge plasma density to bulk electron density, from G&M infinitely long
cylindrical discharge

  DAA = (2/3)*sqrt(k^3/(pi^3*mgas))*(sqrt(T)/(y(4)*k*(2*radAr)^2));
%  DKn = (k*T/(mgas*y(4)*utherm*pi*(2*radAr)^2));
%  DKn = utherm*LMDA/3;
  DKn = sqrt(k*T/mgas)*LMDA/3;
  Deff = 1/(1/DAA+1/DKn);

% MAIN:
  % y(1): n_4s
  % y(2): n_e
  % y(3): n_iz
  % y(4): n_n
  % y(5): Te

  % change in number density of excited state atoms
  dydt(1) = (K1*y(4)*y(2)... %creation/destruction of 4s exciteds via
collisions
         - K2*y(1)*y(2)...  %
         - K4*y(1)*y(2))... %
       - A*y(1)...   %loss of exciteds to spontaneous decay
       - Deff*y(1)/(LMDA^2); %wall losses via diffusion
  % change in number density of electrons
  dydt(2) = (K3*y(2)*y(4)+K4*y(1)*y(2)) -
(hL*AL+hR*AR)*y(2)*sqrt(qe*y(5)/mgas)/vol;
  % change in number density of ions (should be identical to change in
electrons to maintain quasi-neutrality)
  dydt(3) = (K3*y(2)*y(4)+K4*y(1)*y(2)) -
(hL*AL+hR*AR)*y(2)*sqrt(qe*y(5)/mgas)/vol;
  % change in number density of neutral ground-state atoms
  dydt(4) = -K1*y(4)*y(2)...   % loss to exciteds
       + K2*y(1)*y(2)...     % gain from exciteds
       + A*y(1)...      % gain from 4s decay
       - K3*y(4)*y(2);       % loss to ionizations
  % change in bulk electron temperature
  dydt(5) = P_abs/((3/2)*vol*qe*y(2))...%power absorbed term
       - (hL*AL+hR*AR)*uB*(Vs+(5/2)*y(5))/((3/2)*vol)... %wall loss
terms
       -(2/3)*(K3*E_iz*y(4)+K4*(E_iz-E_ex)*y(1)...%energy losses via
ionizations
```

```
            +K1*E_ex*y(4)-K2*E_ex*y(1)...     %energy losses/gains via
exciteds creation/destruction
            +K0*E_elas*y(4))...%energy losses via elastic collisions
between electrons & neutrals
       - (y(5)/y(2))*((K3*y(2)*y(4)+K4*y(2)*y(1)) -
(hL*AL+hR*AR)*y(2)*sqrt(qe*y(5)/mgas)/vol);%other half of d/dt term
that falls out of product rule (dn_e/dt)

end
```

Octave file *d_dtw_oPower.m* used for solving the system of differential equations where power addition is NOT present;

```
% filename: d_dtw_oPower.m
% author: Warner C. Meeks
% contact: wcm994@mst.edu
% advisor: Joshua L. Rovey, (roveyj@mst.edu)
% affiliation: Missouri University of Science and Technology, Aerospace
Plasma Lab, Aerospace Engineering Dept.
% purpose: function called by differential equations solver
% dependencies: none
% NOTES: none

%function dydt = d_dtw_oPower(t,y,P_abs,rate_set) % for MATLAB
function dydt = d_dtw_oPower(y,t) % for OCTAVE
  global rate_set
  disp(t);  % provide output of current step
  fflush(stdout);  % prints 'disp' and 'printf' calls to screen
immediately while in loop rather than wait until loop exit
  dydt = zeros(5,1);
% CONSTANTS:
  HCS = 0.88D-20;  % [m^2]
  k = 1.3807D-23;  % [J/K] Boltzmann's const
  qe = 1.6D-19;  % fundamental charge [coulombs]
  me = 0.91D-30; % electron mass [kg]
  mu0 = pi*4.0D-07;  % Permeability of free space [V-s/A-m]
  M_gas_mol = 39.95;      % mass of gas used [g/mol]
  mgas = M_gas_mol/(1000*6.022D23);  % mass per particle [kg]
  radAr = 71D-12;  % [m] atomic radius of argon neutral
  L = 0.075;     % [m] length of cylindrical device
  R = 0.1525; % [m] radius of cylindrical device
  vol = pi*R^2*L;  % [m^2]volume of plasma assuming thin sheath
  AR = 2*pi*R^2; % [m^2]surface area of top+bottom of cylinder
  AL = 2*pi*R*L; % [m^2]surface area of side walls of cylinder
  LMDA = 1/sqrt((pi/L)^2+(2.405/R)^2);  % effective diffusion length
  E_ex = 12.14;
  E_iz = 15.76;  % from Lieberman pg.81


% DECLARATIONS:
  crs_sec = dlmread('Ar_CS_Rapp.csv',',');
  crs_sec(:,2) = crs_sec(:,2).*HCS;
  sz1 = size(crs_sec);
  area1 = 0.0;
  areaN = 0.0;
  T = 600;  % [K] neutral background temperature


% POWER INPUT:
  %none%


% RATE CONSTANTS:
  K0 = 2.336D-14*y(5)^1.609*exp(0.0618*(log(y(5)))^2-
0.1171*(log(y(5)))^3);  % e+Ar elastic scattering (Lieberman pg.81)
```

```
  E_elas = (3*me/mgas)*y(5);   % mean elastic energy transfer
(Lieberman pg.81)

  K1 = 2.48D-14*y(5)^0.33*exp(-12.78/y(5));  % Ar+e --> Ar*+e
  K2 = 6.88D-16*y(5)^0.33;            % Ar*+e --> Ar+e
  K3 = 2.3D-14*y(5)^0.68*exp(-15.76/y(5)); % Ar+e --> Ar'+2e  '=ionized
%  K4 = (6.8D-15*y(5)^0.67*exp(-4.20/y(5))+1.8D-13*y(5)^0.61*exp(-
2.61/y(5)))/2; % Ar*+e --> Ar'+2e (non-weighted average from Ashida
model)
  K4 = 9.34D-14*y(5)^0.64*exp(-3.405/y(5));  % Ar*+e --> Ar'+2e

  A = rate_set*3.0D07*2*(1/R+1/L)/(y(4)*2.9D-16); %[1/s] Ar* --> Ar+hv
  r=resonance

  Vs = (y(5)/2)*log(mgas/(2*pi*me));  % [V]  estimated voltage drop in
sheath
  uB = sqrt(qe*y(5)/mgas);     % [m/s]Bohm velocity
  utherm = sqrt(8*k*T/(pi*mgas));

  F_E = sqrt(4*crs_sec(:,1)./(pi*y(5)^3)).*exp(-crs_sec(:,1)./y(5));
  integrand = crs_sec(:,2).*F_E;

  % descrete integration under CS data curve (sum of trapazoidal areas)
  for c0 = 1:(sz1(1)-1)
    areaN = (crs_sec(c0+1,1)-
crs_sec(c0,1))*(integrand(c0+1)+integrand(c0))/2;
    area1 = area1 + areaN;
  end
  sgma = area1;
%  sgma = 2.9D-16;
  lmda = 1/(y(4)*sgma); % [m]  estimated ion-neutral collision mean
free path
  hL = 0.86/sqrt(3.0+L/(2*lmda));% [m^-3/m^-3] ratio of axial sheath
edge plasma density to bulk electron density, from Godyak and Maximov
plane parallel discharge
  hR = 0.80/sqrt(4.0+R/lmda);  % [m^-3/m^-3] ratio of radial sheath
edge plasma density to bulk electron density, from G&M infinitely long
cylindrical discharge

  DAA = (2/3)*sqrt(k^3/(pi^3*mgas))*(sqrt(T)/(y(4)*k*(2*radAr)^2));
%  DKn = (k*T/(mgas*y(4)*utherm*pi*(2*radAr)^2));
%  DKn = utherm*LMDA/3;
  DKn = sqrt(k*T/mgas)*LMDA/3;
  Deff = 1/(1/DAA+1/DKn);

% MAIN:
  % y(1): n_4s
  % y(2): n_e
  % y(3): n_iz
  % y(4): n_n
  % y(5): Te

  % change in number density of excited state atoms
  dydt(1) = (K1*y(4)*y(2)... %creation/destruction of 4s exciteds via
collisions
          - K2*y(1)*y(2)...  %
```

```
          - K4*y(1)*y(2))... %
        - A*y(1)...    %loss of exciteds to spontaneous decay
        - Deff*y(1)/(LMDA^2); %wall losses via diffusion
  % change in number density of electrons
  dydt(2) = (K3*y(2)*y(4)+K4*y(1)*y(2)) -
(hL*AL+hR*AR)*y(2)*sqrt(qe*y(5)/mgas)/vol;
  % change in number density of ions (should be identical to change in
electrons to maintain quasi-neutrality)
  dydt(3) = (K3*y(2)*y(4)+K4*y(1)*y(2)) -
(hL*AL+hR*AR)*y(2)*sqrt(qe*y(5)/mgas)/vol;
  % change in number density of neutral ground-state atoms
  dydt(4) = -K1*y(4)*y(2)...   % loss to exciteds
       + K2*y(1)*y(2)...     % gain from exciteds
       + A*y(1)...      % gain from 4s decay
       - K3*y(4)*y(2);    % loss to ionizations
  % change in bulk electron temperature
  dydt(5) = -(hL*AL+hR*AR)*uB*(Vs+(5/2)*y(5))/((3/2)*vol)...  %wall
loss terms
       -(2/3)*(K3*E_iz*y(4)+K4*(E_iz-E_ex)*y(1)...%energy losses via
ionizations
            +K1*E_ex*y(4)-K2*E_ex*y(1)...    %energy losses/gains via
exciteds creation/destruction
            +K0*E_elas*y(4))...%energy losses via elastic collisions
between electrons & neutrals
       - (y(5)/y(2))*((K3*y(2)*y(4)+K4*y(2)*y(1)) -
(hL*AL+hR*AR)*y(2)*sqrt(qe*y(5)/mgas)/vol);%other half of d/dt term
that falls out of product rule (dn_e/dt)

end
```

APPENDIX B

SUPPORT FILES USED TO ITERATIVELY RUN XOOPIC FOR USER SPECIFIED TIME-VARYING ELECTROMAGNETIC FIELDS

Bash-file *tasks.sh* that executes XOOPIC input file *iterFRCHX.inp* to a specified number of steps, dumps output, runs the Octave script *getAVGvel.m*, and repeats with updated electromagnetic fields;

```
#!/bin/bash
###  filename: run_iterative.sh
###  author:   Warner C. Meeks
###  contact:  wcm994@mst.edu
###  advisor:  Joshua L. Rovey (roveyj@mst.edu)
###  affiliation:Missouri University of Science and Technology,
Aerospace Plasma Lab, Aerospace Engineering Dept.
###  purpose:  Shell script to run XOOPIC iteratively updating magnetic
and electric fields at each new run to simulate time-vary fields, which
XOOPIC cannot handle natively.
###  references: John Verboncoeur (johnv@msu.edu), helped to explain
XOOPIC flag options/capabilities
###  dependencies:requires 'Ifile.txt' and 'dIdtfile.txt' produced by
the Matlab script 'piecewisefields.m'

for ((c1=0;c1<2000;c1++))
do
  oopicDIR=$HOME/Documents/XOOPIC/xoopic
  inputDIR=$oopicDIR/my_input
  outputDIR=$inputDIR/step1ns_stop2us_wIons
  inputfile=$inputDIR/iterFRCHX.inp
  tmpfile1=$inputDIR/tmpinput1.inp
  tmpfile2=$inputDIR/tmpinput2.inp
  msgs=$inputDIR/iterationlog.txt

  # number of iterations between particle dumps in
xoopic/otools/diagn.cpp
  # dt = 1E-11 s (this is set by dt in input file)
  # $c1*$stopAT*dt (this would be the current time during simulation in
seconds)
  stopAT=100

  # 'cat' indexing starts at index '0'
  B=(`cat Bt.txt`)
  E=(`cat Et.txt`)

  # velocity average file always needs re-initiallized with '0' in the
first line and nothing else
  Vynew=(`cat totvelavg.txt`)

  #rm -f $msgs

  # iterative filename declaration
  filePOS=$outputDIR/$c1"pos.txt"
  fileVEL=$outputDIR/$c1"vel.txt"

  echo "beginning run #$c1... "

  printf "\n\n\n**************\nStart of iteration
($c1)\n**************\n" >> $msgs
```

```
   awk '/B01/ {gsub(/iterBt/,s1)}; {print}' s1="${B[$c1]}" $inputfile >
$tmpfile1
   awk '/E3init/ {gsub(/iterEt/,s1)}; {print}' s1="${E[$c1]}" $tmpfile1
> $tmpfile2
   awk '/v2drift/ {gsub(/V2D/,s1)}; {print}' s1="${Vynew[$c1]}"
$tmpfile2 > $tmpfile1
   ../xoopic -i $tmpfile1 -nox -s $stopAT >> $msgs

   echo "moving output files..."
   mv pos.txt $filePOS
   mv vel.txt $fileVEL

   # run Octave to calc new input v2drift velocity
   cd $outputDIR
   octave -qf getAVGvel.m $c1
   cd ..

done

exit 0
```

XOOPIC input file *iterFRCHX.inp* with dummy names, 'iterBt', 'iterEt', and 'V2D' which are replaced with updated values during the loop in *tasks.sh*.

```
iterFRCHX.inp
{
  filename: my_FRCHX01.inp
  author:  Warner C. Meeks
  contact: wcm994@mst.edu
  advisor:   Joshua L. Rovey (roveyj@mst.edu)
  affiliation:  Missouri University of Science and Technology,
Aerospace Plasma Lab, Aerospace Engineering Dept.
  purpose: Mock up of FRCHX device to model EEDF evolution at early
times (i.e., t<1e-6 s).
  references: >>J.P. Verboncoeur, A.B. Langdon and N.T. Gladd, "An
Object-Oriented Electromagnetic PIC Code," Comp. Phys. Comm., 87,
May11, 1995, pp. 199-211
                  Input file adapted from a demo input file supplied
with XOOPIC.
              >>C. Grabowski, et al, "FRC Lifetime Studies for the
Field Reversed Configuration Heating Experiment (FRCHX)," IEEE-Pulsed
Power Conference, 2011
              >>C. Grabowski, et al, "FRC Compression Heating
Experiment (FRCHX) at AFRL," IEEE-Pulsed Power Conference, 2009
}
Variables
{
  sclr = 16 // scales the grid and all geometries to a certain number
of cells
         // sclr=100 runs considerably slower than sclr=10
  electronMass = 9.1093897e-31
  unitCharge = electronMass * 1.75881962e11
  electronCharge = -1.0 * unitCharge
  ionCharge = unitCharge
  unitMassMKS = electronMass / 5.48579903e-04
  atomicMass = unitMassMKS * 1.008    // H=1.008, He=4.003, Ar=39.95,
Ne=20.18, N=14.01, Xe=131.3, Li=6.94
  L = 0.364/2   //length of FRCHX
  R = 0.065   //averaged radius of theta-pinch coil
  LRratio = 3 // approximate to provide square-ish grid    NOTE:needs
to be an integer
//mu0 = PI*4e-7
//period = 4e-6  // [s]
//freq = 1/period  // [1/s]
}
Region
{
Grid
{
  Geometry = 1
  J = LRratio*sclr   //horizontal grid resolution (z)
  x1s = 0.0 //horizontal physical space start (m)
  x1f = L   //horizontal physical space end (m)
  n1 = 1.0
  K = sclr    //vertical grid resolution (r)
  x2s = 0.0 //vertical physical space start (m)
```

```
   x2f = R   //vertical physical space end (m)
   n2 = 1.0
}
Control
{
   dt = 1.0E-11
   ElectrostaticFlag=1
   B01 = iterBt     // [Tesla]     x1:x, x2:y, x3:z
   E3init = iterEt*x2 // for 0.5 T
}
MCC
{
   gas = H   // H, He, Ar, Ne, N, Xe, Li
   pressure = .05
   eSpecies = electrons
   iSpecies = ions
}
Species
{
    name = electrons
    m = electronMass
    q = electronCharge
   collisionModel = 1
}
Species
{
   name = ions
    m = atomicMass
    q = ioncharge
   collisionModel = 2
}
Load
{
   speciesName = electrons
   density = 1e11
   x1MinMKS = 0//0.1
   x2MinMKS = 0//0.01
   x1MaxMKS = L//0.12
   x2MaxMKS = R//0.015
   np2c = 1e6
   v2drift = V2D
// v3drift = V3D
// temperature = 5.13399e5 // 5.13399 m/s corresponts to 0.5 eV
// temperature = 1.0268e6     // 1.0268e6 m/s corresponds to 2 eV
// temperature = 1.62351e6 // 1.62351 m/s corresponds to 5 eV
// temperature = 2.56699e6 // 2.56699e6 m/s corresponds to 12.5 eV
// units = EV
}
Load
{
   speciesName = ions
   np2c = 1e6
}
Conductor // left wall
{
   j1 = 0
```

```
   k1 = 0
   j2 = 0
   k2 = sclr
   normal = 1
// reflection = 1
}
Dielectric  // top wall
{
   j1 = 0
   k1 = sclr
   j2 = LRratio*sclr
   k2 = sclr
   normal = -1
// QuseFlag=0
// reflection = 1
}
Conductor // right wall
{
   j1 = LRratio*sclr
   k1 = 0
   j2 = LRratio*sclr
   k2 = sclr
   normal = -1
// reflection = 1
}
Dielectric  // bottom wall
{
   j1 = 0
   k1 = 0
   j2 = LRratio*sclr
   k2 = 0
   normal = 1
   reflection = 1
}
}
```

Octave file *getAVGvel.m* that receives the dumped particle velocity data from XOOPIC, calculates the average, and writes this data out to a text file, *totvelavg.txt*.

```
%% filename: getAVGvel.m
% author:  Warner C. Meeks
% contact: wcm994@mst.edu
% advisor: Joshua L. Rovey (roveyj@mst.edu)
% affiliation:  Missouri University of Science and Technology,
Aerospace Plasma Lab, Aerospace Engineering Dept.
% purpose: Read data output files from XOOPIC
% references: none
% dependencies: none
% NOTES: made to run in Octave

clear all

%% CONSTANTS:
    me=9.11D-31;   % [kg]  mass of electron
    qe=1.6D-19;   % [C]   fundamental charge
    c=299792458; % [m/s]speed of light
    C1=argv(){1};
    C1


%% TIME MANAGEMENT:
  t1=clock; % for program duration checking only, not used in
calculations


%% INITIAL CONDITIONS: {none}


%% MAIN:
    % Importing velocity and position files
    Vname=[num2str(C1),'vel.txt'];
    temp1=dlmread(Vname,',');
    correction=c.*temp1./sqrt(temp1.^2+c^2);  # gamma factor correction
for faster-than-light speeds
    avgvel=mean(abs(correction));

    totvel=sqrt(avgvel(1)^2+avgvel(2)^2+avgvel(3)^2);

    dlmwrite("../totvelavg.txt",totvel,"-append");

%% TIME MANAGEMENT (cont.):
  t2=clock; % for program duration checking only, not used in
calculations
  run_time=t2-t1;
  %disp('[hr:min:sec]');
  %disp(run_time(4:end));
```

APPENDIX C

SINGLE PARTICLE MODEL FOR USER SPECIFIED TIME-VARYING ELECTROMAGNETIC FIELDS

Matlab file *ExBtrajectory.m* for simple electron motion in perpendicular field topology.

```
% filename: ExBtrajectory.m
% author: Warner C. Meeks
% contact: wcm994@mst.edu
% advisor: Joshua L. Rovey, (roveyj@mst.edu)
% affiliation: Missouri University of Science and Technology, Aerospace
Plasma Lab, Aerospace Engineering Dept.
% purpose: run and plot (3D, movie) a single charged particles motion
in an ideal theta-pinch (solenoid)
% dependencies: Vxy.m
% NOTES: none

%% Prelims
close all
clear all
clc

global Q IC me wc


%% Definitions
rpd=pi/180.0;
dpr=180.0/pi;

% For using singly-charged Argon ion
%MW = 39.95;  % [g/mol]
%N = 6.022e23;% [part/mol]
%m = (MW/N)/1000.0;% [kg/part]

me=9.11e-31;  % [kg]
q=1.60e-19; % [C] fundamental charge
z=1; % charge lvl
sign=-1;
Q=sign*q*z;
Ig=15.47; % ionization potential for gaseous deuterium

% Time frame
dt=1e-10;
subdt=1e-11;
ts=0;
tf=1.2e-6;  % [sec]
mainT=ts:dt:tf-dt; % [sec]
mTsize=size(mainT);
allT=ts:subdt:(tf-subdt);
Tsize=size(allT);
freq=250000;  % [Hz]
dr=0.0001;
Rpos=0:dr:0.065; % [m]

Bpi=0.5;
Bbias=0.5;

szBbias=size(Bbias);
```

```
%% Calculations
for i=1:szBbias(2)
  i
  Bt=-Bpi*sin(2*pi*freq.*mainT)+Bbias(i);
  Etemp=Bpi*2*pi*freq*cos(2*pi*freq.*mainT);

  Et=Etemp'*Rpos./2; % -(dB/dt)*r/2

  substeps=int32(dt/subdt);

  Vxy=NaN(Tsize(2),2);

  for j=1:(mTsize(2)-1)
    j
    % Initial conditions, IC= { [r(m); v(m/s); E(V/m); B(T)] }
    % IC needs to reflect new initial velocities from previous solve...

    if j==1
      xyz(:,j)=[0,0.001,0]; % initial position
      v=[0,0,0];
      E=[Et(j,round(xyz(2)*(1/dr))),0,0];
      B=[0,0,Bt(j)];
    else
      v=[Vall(end,1),Vall(end,2),0];
      E=[Et(j,round(xyz(2,j)*(1/dr))),0,0];
      B=[0,0,Bt(j)];
    end

    IC=[xyz(1,j),xyz(2,j),xyz(3,j);v;E;B];

    myE(j)=E(1);

    wc=abs(Q)*IC(4,3)/me;

    v0=[IC(2,1); IC(2,2)];% IC(2,3)];

    subT=mainT(j):subdt:(mainT(j+1)-subdt);

    [Tall,Vall]=ode45('Vxy',subT,v0);

    Vx=Vall(end,1);
    Vy=Vall(end,2);

    xyz(1,j+1)=Vx*(subT(end)-subT(1))+xyz(1,j);
    xyz(2,j+1)=Vy*(subT(end)-subT(1))+xyz(2,j);
    xyz(3,j+1)=0;

    Vxy((substeps*(j-1)+1):(substeps*(j)),:)=Vall;

  end

  Vperp=sqrt(Vxy(:,1).^2+Vxy(:,2).^2);
  singleE(:,i)=(me/(2*q)).*Vperp.^2;

end
```

```
%% Plotting

[x,z]=meshgrid(-13:0.1:13,-13:0.1:13);
szX=size(x);
szZ=size(z);

Y=18.2.*ones(szX(2),szZ(2));

x1=0:0.1:6.49;
x2=6.5:0.1:19.5;
x3=19.51:0.1:26.0;

z1=13.*ones(1,65);
z2=[sqrt(6.5^2-(fliplr(x1)).^2),6.5,sqrt(6.5^2-x1.^2)]+13;
z3=13.*ones(1,65);

Z=round([z1,z2,z3].*10);

for i=1:szX(2)
  Y(i,Z(i):end)=-18.2;
end

avi1 = avifile('ThetaPinch_ExBdrift.avi','fps',20);

for i=1:10:(mTsize(2)-1)
  i
  figure(1)
  subplot(2,3,[1,2,4,5])
  scatter3(xyz(1,i)*100,xyz(3,i)*100,xyz(2,i)*100,20,'red','filled')
  hold on

mesh(x(68:200,110:196),Y(68:200,110:196),z(68:200,110:196),'FaceColor',
'none','EdgeColor',[0.6 0.6 0.7])
  hold on
  plot3(xyz(1,1:i).*100,xyz(3,1:i).*100,xyz(2,1:i).*100)
  hold off
  axis([-2 8 -20 20 -7 7])
  view(-36,-10)
  title(['Particle drift in typ. \theta-pinch.  time:
',num2str(mainT(i)./1E-6),' \mus'],'FontName','Arial','FontSize',14);
%  xlabel('radial (cm) parallel to \bf
E','FontName','Arial','FontSize',12)
  xlabel('x (cm)','FontName','Arial','FontSize',12)
  ylabel('axial (cm)','FontName','Arial','FontSize',12)
%  zlabel('radial (cm) perp. to \bf E','FontName','Arial','FontSize',12)
  zlabel('y (cm)','FontName','Arial','FontSize',12)
  set(gca,'FontName','Arial','FontSize',12)
  set(gcf,'Color',[1,1,1])
  grid('on')

  subplot(2,3,3)
  limitoffset=1.2;
  [AX,H1,H2]=plotyy(mainT./1E-6,Bt,mainT./1E-6,Etemp./2E5);
%  [AX,H1,H2]=plotyy(mainT./1E-6,Bt,mainT./1E-6,[myE,myE(end)]./1E5);
  grid('on')
```

```
  hold on
  scatter(mainT(i)./1E-6,Bt(i),30,'red')
  line([mainT(i)./1E-6,mainT(i)./1E-6],
[0,1],'LineWidth',1,'Color','red')
  hold off
  set(get(AX(1),'Ylabel'),'String','B(t) (T)')
  set(get(AX(2),'Ylabel'),'String','E(t) at r=1cm (kV/cm)')
%  set(get(AX(2),'Ylabel'),'String','E(t) at e^{-} position (kV/cm)')
  set(AX(1),'YLim',[0 0.5],'XLim',[0 1.2])
  set(AX(2),'YLim',[limitoffset*min(Etemp./2E5)
limitoffset*max(Etemp./2E5)],'XLim',[0 1.2])
%  set(AX(2),'YLim',[2*min(myE)/1E5 1.2*max(myE)/1E5],'XLim',[0 1.2])

  subplot(2,3,6)
  plot(mainT./1E-6,singleE(1:10:end)')
%  semilogy(mainT./1E-6,singleE(1:10:end)')
  grid('on')
  hold on
  scatter(mainT(i)./1E-6,singleE(i*10),30,'red')
  line([mainT(i)./1E-6,mainT(i)./1E-6],
[0,max(singleE)],'LineWidth',1,'Color','red')
  hold off
  ylabel('energy (eV)')
  xlabel('time \mus')
  axis([0 1.2 0 max(singleE)])

  frame = getframe(figure(1));
  avi1 = addframe(avi1,frame);
end


%% Exit Conditions
avi1 = close(avi1);
```

Matlab function file *Vxy.m* called by *ExBtrajectory.m* containing the system of two first order coupled differential equations of motion.

```
function vdot = Vxy(t,v)
%  filename: Vxy.m
%  author: Warner C. Meeks
%  contact: wcm994@mst.edu
%  advisor: Joshua L. Rovey, (roveyj@mst.edu)
%  affiliation: Missouri University of Science and Technology, Aerospace
Plasma Lab, Aerospace Engineering Dept.
%  purpose: function file with system of 2 equations of motion solved
via an ODE solver
%  dependencies: none
%  NOTES: none

    global Q IC me wc
    vdot = zeros(2,1);

    vdot(1) = (Q/me)*IC(3,1) + wc*v(2);
    vdot(2) = (Q/me)*IC(3,2) - wc*v(1);

end
```

BIBLIOGRAPHY

[1] Samukawa, S., & Mieno, T., "*Pulse-time modulated plasma discharge for highly selective, highly anisotropic and charge-free etching*," Plasma Sources Sci. Technol., IOP, Vol.5, No.2, pp. 132-138, 1996.

[2] Hopwood, J., "*Review of inductively coupled plasmas for plasma processing*," Plasma Sources Sci. Technol., IOP, Vol.1, No.2, pp. 109-116, 1992.

[3] Brown, D.L., Beal, B.E., & Haas, J.M., "Air Force Research Laboratory High Power Electric Propulsion Technology Development," Edwards AFB, CA, No. 2-0102, AFRL, 2009

[4] Dailey, C.L., & Lovberg, R.H., "The PIT MkV Pulsed Inductive Thruster," Lewis Research Center, No. 191155, National Aeronautics and Space Administration, 1993

[5] Meyer, M., Johnson, L., Palaszewski, B., et. al., "In-space Propulsion Systems Roadmap," NASA Headquarters, Washington, D.C. 20546, No. TA02, National Aeronautics and Space Administration, 2010

[6] Tuszewski, M., "*Field Reversed Configurations*," Nuclear Fusion, IAEA, Vol.28, No.11, pp. 2033-2092, 1988.

[7] Armstrong, W.T., Cochrane, J.C., Commisso, R.J., et. al., "*Theta-pinch ionization for field-reversed configuration formation*," Appl. Phys. Lett., AIP, Vol.38, No.9, pp. 680-682, 1981.

[8] Armstrong, W.T., Linford, R.K., Lipson, J., et. al., "*Field-Reversed Experiments (FRX) on Compact Toroids*," Physics of Fluids, AIP, Vol.24, No.11, pp. 2068-2089, 1981.

[9] Kirtley, D.E., "Study of the Synchronous Operation of an Annular Field Reversed Configuration Plasma Device," Dept. of Aerospace Engineering, University of Michigan, Ann Arbor, MI, 2008

[10] Russell, D., Poylio, J.H., Goldstein, W., et. al., "The Mark VI Pulsed Inductive Thruster," *Space Conference and Exhibit*, San Diego, California, 2004.

[11] Polzin, K.A., "*Scaling and Systems Considerations in Pulsed Inductive Plasma Thrusters*," IEEE - Transactions on Plasma Science, IEEE, Vol.36, No.5, pp. 2189-2198, 2008.

[12] Polzin, K.A., "*Comprehensive Review of Planar Pulsed Inductive Plasma Thruster Research and Technology*," J. Propuls. Power, AIAA, Vol.27, No.3, p. pp. 513-531, May-June 2011.

[13] Frisbee, R.H., & Mikellides, I.G., "The Nuclear-Electric Pulsed Inductive Thruster (NuPIT): Mission Analysis for Prometheus," *41st Joint Propulsion Conference and Exhibit*, Tucson, AZ, 2005.

[14] Koelfgen, S.J., & Hawk, C.W., "A Plasmoid Thruster For Space Propulsion," *39th Joint Propulsion Conference and Exhibit*, Hustsville, AL, 2003.

[15] Slough, J., Kirtley, D., & Weber, T., "Pulsed Plasmoid Propulsion: The ELF Thruster," *31st International Electric Propulsion Conference*, Ann Arbor, MI, 2009.

[16] Choueiri, E.Y., & Polzin, K.A., "*Faraday Acceleration with Radio-Frequency Assisted Discharge*," J. Propuls. Power, AIAA, Vol.22, No.3, pp. 611-619, 2006.

[17] Hallock, A.K., Choueiri, E.Y., & Polzin, K.A., "Current Sheet Formation in a Conical Theta Pinch Faraday Accelerator with Radio-frequency Assisted Discharge," *30th International Electric Propulsion Conference*, Florence, Italy, 2007.

[18] Steinhauer, L.C., "*Review of field-reversed configurations*," Physics of Plasmas, AIP, Vol.18, No.7, pp. 070501-070501, 2011.

[19] Steinhauer, L.C., Milroy, R.D., & Slough, J.T., "*A model for inferring transport rates from observed confinement times in field-reversed configurations*," Physics of Fluids, AIP, Vol.28, No.3, pp. 888-897, 1985.

[20] Niemela, C.S., & Kirtley, D., "Initial results on an Annular Field Reversed Configuration Plasma Translation Experiment," AFRL Edwards, CA, Contract No. FA9300-06-C-0023, AFRL, 2008

[21] V. Surla, M. A. Jaworski, T. K. Gray, et al., "*Lithium research as a plasma facing component material at the University of Illinois*," Thin Solid Films, Elsevier B.V., Vol.518, No.22, 6663, 2010.

[22] Xu Feng-zhi, Chen Geng-hua, Yang Qian-sheng, et al., "*Superconducting film injected by ions from pulsed energetic dense plasma source*," J. Chinese Phys., IOP & Chin. Phys. Soc., Vol.10, No.11, 1049, 2001.

[23] N. Takeuchi, K. Yasuoka, & I. Shozo, "Surface modification of thin dielectric materials by compact theta-pinch plasma," *Intl. Conference On Plasma Sci.*, Monterey, CA, 2005.

[24] W. T. Armstrong, J. C. Cochrane, R. J. Commisso, et al., "*Theta-pinch ionization for field-reversed configuration formation*," Appl. Phys. Lett., AIP, Vol.38, No.9, 680, 1981.

[25] J. M. Taccetti, T. P. Intrator, G. A. Wurden, et al., "*FRX-L: A field-reversed configuration plasma injector for magnetized target fusion*," Rev. Sci. Instrum., AIP, Vol.74, No.10, 4314, 2003.

[26] C. Grabowski, J. Degnan, M. Babineau, et al., "FRC compresion Heating Experiment (FRCHX) at AFRL," *Pulsed Power Conference*, Albuquerque, NM, 2007.

[27] A. K. Hallock, E. Y. Choueiri, & K. A. Polzin, "Current Sheet Formation in a Conical Theta Pinch Faraday Accelerator with Radio-frequency Assisted Discharge," *30th International Electric Propulsion Conference*, Florence, Italy, 2007.

[28] C. S. Niemela, & L. B. King, "Numerical optimization of an annular field reversed configuration translation experiment," *31st International Electric Propulsion Conference*, University of Michigan, Ann Arbor, MI, 2009.

[29] J. S. White, & A. Scheeline, "*Sampling and Excitation of Refractory Solids with a Theta Pinch Discharge Designed as an Atomic Emission Source*," Analytical Chem., American Chem. Soc., Vol.59, No.2, 305, 1987.

[30] P. D. Pedrow, & A. M. Nasiruddin, "*Experimental Study of CF4 Conical Theta Pinch Plasma Expanding into Vacuum*," Transactions on Plasma Science, IEEE, Vol.17, No.1, 17, 1989.

[31] M. Tuszewski, "*Field Reversed Configurations*," Nuclear Fusion, IAEA, Vol.28, No.11, 2033, 1988.

[32] L. C. Steinhauer, "*Review of field-reversed configurations*," Physics of Plasmas, AIP, Vol.18, No.7, 070501, 2011.

[33] D. Kirtley, A. D. Gallimore, J. Haas, et al., "High Density Magnetized Toroid Formation and Translation within XOCOT: An Annular Field Reversed Configuration Plasma Concept," *30th Intl. Electric Propulsion Conference*, , Florence, Italy, 2007.

[34] A. K. Hallock, E. Y. Choueiri, & K. A. Polzin, "Current Sheet Formation in a Conical Theta Pinch Faraday Accelerator with Radio-frequency Assisted Discharge," *44th Joint Propulsion Conference*, Hartford, CT, 2008.

[35] E. M. Little, W. E. Quinn, & F. L. Ribe, "*Effects of Ionization and Magnetic Initial Conditions on a Magnetically Compressed Plasma (Scylla)*," Phys. Fluids, AIP, Vol.4, No.6, 711, 1961.

[36] R. J. Commisso, W. T. Armstrong, J. C. Caldwell, et al., "The initial ionization stage of FRC formation," *1st Compact Toroid Symposium*, Los Alamos, NM, 1980.

[37] R. D. Milroy, & J. U. Brackbill, "*Numerical Studies of a field-reversed theta-pinch plasma*," Physics of Fluids, AIP, Vol.25, No.5, 775, 1982.

[38] D. E. Kirtley, "Study of the Synchronous Operation of an Annular Field Reversed Configuration Plasma Device," Dept. of Aerospace Engineering, University of Michigan, Ann Arbor, MI, 2008

[39] T. S. Green, & A. A. Newton, "*Diffusion of Antiparallel Bias Magnetic Field during the Initial Stages of a Theta-Pinch*," Phys. Fluids, AIP, Vol.9, No.7, 1386, 1966.

[40] W. T. Armstrong, R. K. Linford, J. Lipson, et al., "*Field-Reversed Experiments (FRX) on Compact Toroids*," Physics of Fluids, AIP, Vol.24, No.11, 2068, 1981.

[41] C. Grabowski, J. H. Degnan, D. J. Amdahl, et al., "FRC Lifetime studies for the field reversed configuration heating experiment (FRCHX)," *53rd Plasma Physics Meeting*, Salt Lake City, UT, 2011.

[42] G. A. Wurden, T. P. Intrator, S. Y. Zhang, et al., "FRC plasma studies on the FRX-L plasma injector for MTF," *Fusion Energy Conference*, Vilamoura, Portugal, 2004.

[43] Ashida, S., Shim, M.R., & Lieberman, M.A., "*Measurements of pulsed-power modulated argon plasmas in an inductively coupled plasma source*," J. Vac. Sci. Technol. A, AVS, Vol.14, No.2, pp. 391-397, 1996.

[44] Sakuta, T., Oguri, S., Takashima, T., et. al., "*Effects of plasma diameter and operating frequency on dynamic behavior of induction thermal plasma*," Plasma Sources Sci. Technol., IOP, Vol.2, No., pp. 67-71, 1993.

[45] Niemela, C.S., & King, L.B., "Numerical optimization of an annular field reversed configuration translation experiment," *International Electric Propulsion Conference*, University of Michigan, Ann Arbor, MI, 2009.

[46] Milroy, R.D., & Brackbill, J.U., "*Numerical Studies of a field-reversed theta-pinch plasma*," Physics of Fluids, AIP, Vol.25, No.5, pp. 775-783, 1982.

[47] Ashida, S., Lee, C., & Lieberman, M.A., "*Spatially averaged (global) model of time modulated high density argon plasmas*," J. Vac. Sci. Technol. A, AVS, Vol.13, No.5, pp. 2498-2507, 1995.

[48] Lee, C., Graves, D.B., Lieberman, M.A., et. al., "*Global Model of Plasma Chemistry in a High Density Oxygen Discharge*," J. Electrochem. Soc., ECS, Vol.141, No.6, pp. 1546-1555, 1994.

[49] Lee, C., & Lieberman, M.A., "*Global model of Ar, O_2, Cl_2, and Ar/O_2 high-density plasma discharges*," J. Vac. Sci. Technol. A, AVS, Vol.13, No.2, pp. 368-380, 1995.

[50] Lieberman, M.A., & Ashida, S., "*Global models of pulse-power-modulated high-density, low-pressure discharges*," Plasma Sources Sci. Technol., IOP, Vol.5, No.2, pp. 145-158, 1996.

[51] Meeks, W.C., Pahl, R.A., & Rovey, J.L., "Investigation of Pre-ionization Characteristics in Heavy Gas Pulsed Inductive Plasmas via Numerical Modeling," *47th Joint Propulsion Conference & Exhibit*, San Diego, CA, 2011.

[52] Lieberman, M.A., & Lichtenberg, A.J., in *Principles of Plasma Discharges and Materials Processing* (John Wiley & Sons, Inc., Hoboken, 2005), p. 134.

[53] Rapp, D., & Englander-Golden, P., "*Total Cross Sections for Ionization and Attachment in Gases by Electron Impact. I. Positive Ionization*," J. Chem. Phys., AIP, Vol.43, No.5, pp. 1464-1479, 1965.

[54] Behle, S., Brockhaus, A., & Engemann, J., "*Time-resolved investigations of pulsed microwave excited plasmas*," Plasma Sources Sci. Technol., IOP, Vol.9, No.1, pp. 57-67, 2000.

[55] Hebner, G.A., & Fleddermann, C.B., "*Characterization of pulse-modulated inductively coupled plasmas in argon and chlorine*," J. Appl. Phys., AIP, Vol.82, No.6, pp. 2814-2821, 1997.

[56] Ishigaki, T., Okada, N., Ohashi, N., et. al., "*Nonthermal and nonequilibrium effects in high-power pulsed ICP and application to surface modification of materials*," Pure Appl. Chem., IUPAC, Vol.74, No.3, pp. 435-439, 2002.

[57] J. P. Verboncoeur, A. B. Langdon, & N. T. Gladd, "*An object-oriented electromagnetic PIC code*," Comp. Phys. Comm., Elsevier Sci., Vol.87, No., 199, 1995.

[58] J. P. Verboncoeur, "*Particle simulation of plasmas: review and advances*," Plasma Phys. Control. Fusion, IOP, Vol.47, No.5A, A231, 2005.

VITA

Born and raised in northern St. Louis, Missouri, Warner graduated from Hazelwood Central highschool in 2001. After working in the blue-collar environment for a few years he decided to get further education and began studies at St. Louis Community College with the intent to transfer to a four year institution. He transferred to Missouri University of Science and Technology in 2007 (at the time University of Missouri – Rolla) along with his wife who pursued a Bachelor of Arts in History. Warner graduated from Missouri S&T in 2010 with a Bachelor of Science in Aerospace Engineering. In the last year of his undergraduate he began doing research under a (at the time) fairly new professor, Dr. Josh Rovey. Upon graduating with his B.S. he came on full-time to pursue a graduate education under Dr. Rovey in Aerospace Engineering. Warner has now obtained his Master's Degree in Aerospace Engineering in December of 2012. This work represents what he hopes to be a halfway point to a Ph.D in the same.

Warner has been a tinker-er and daydreamed of traveling the universe his entire life. He sees the space industry (and aircraft industry, for that matter) stagnating and in need of new breakthroughs in science and technology. Confident these breakthroughs are around the corner he has high hopes for both his and the coming generations to make the visions found in space genre science-fiction every bit a reality as were made the dreams of da Vinci and Galileo.